

RICE UNIVERSITY

3D optical lattice system for ultra-cold Lithium 6

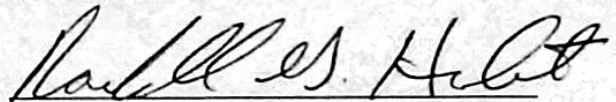
by

Tsung-Lin Yang

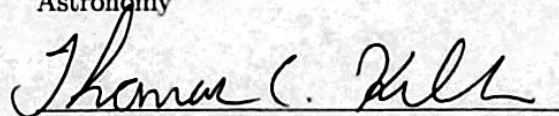
A THESIS SUBMITTED
IN PARTIAL FULFILLMENT OF THE
REQUIREMENTS FOR THE DEGREE

Master of Science

APPROVED, THESIS COMMITTEE:



Randall G. Hulet, Chair
Fayez Sarofim Professor of Physics and
Astronomy



Thomas C. Killian
Professor of Physics and Astronomy



Pengcheng Dai
Professor of Physics and Astronomy

Houston, Texas

April, 2014

RICE UNIVERSITY

3D optical lattice system for ultra-cold Lithium 6

by

Tsung-Lin Yang

A THESIS SUBMITTED
IN PARTIAL FULFILLMENT OF THE
REQUIREMENTS FOR THE DEGREE

Master of Science

APPROVED, THESIS COMMITTEE:

Randall G. Hulet, Chair
Fayez Sarofim Professor of Physics and
Astronomy

Thomas C. Killian
Professor of Physics and Astronomy

Pengcheng Dai
Professor of Physics and Astronomy

Houston, Texas

April, 2014

ABSTRACT

3D optical lattice system for ultra-cold Lithium 6

by

Tsung-Lin Yang

Optical lattice experiments have proved to be a versatile tool for studying strongly correlated quantum systems. The motivation behind these experiments is to use the cold atoms to emulate a solid state system for which the Hamiltonian is analytically or numerically non-solvable. In our experiment, we construct a 3D simple cubic lattice system which realizes the Fermi-Hubbard model and provides us the opportunity to study the antiferromagnetic (AFM) insulator phase. In order to establish evaporative cooling in the optical lattice and to enlarge the size of the AFM phase, we implement a compensation potential additional to the standard lattice beam. In this thesis, I will present detailed steps to construct and calibrate the compensated 3D optical lattice system.

Contents

Abstract	ii
List of Illustrations	vi
List of Tables	viii
1 Introduction	1
1.1 Properties of ${}^6\text{Li}$	2
1.2 Dipole force	3
1.3 Outline of the thesis	4
2 Experimental Sequence	5
2.1 Zeeman slower, red MOT, UV MOT	5
2.2 Cross-beam dipole trap	6
2.3 Compensated optical lattice	6
3 High dynamic range intensity stabilized dipole trap	8
3.1 Design and Setup	8
3.1.1 Gain for the photodiodes	11
3.1.2 Calibration of the intensity servo	13
3.1.3 PI corner gain for feedback	13
3.1.4 Bandwidth of the system	15
3.1.5 Discussion on noise Source	18
3.2 Degenerate Fermi gas	18
4 Compensated 3D Lattice	20

4.1	Introduction to optical lattice	20
4.2	Compensated optical lattice	22
4.3	Green and IR laser system	25
4.3.1	Intensity stabilization	25
4.3.2	Calibration of the intensity servo	28
4.3.3	Fiber interlock	29
4.4	Lattice Assembly	30
4.4.1	Picomotor mirror mount	30
4.4.2	Liquid crystal retarder	30
4.5	Beam Profile and alignment	32
4.5.1	Alignment on the test bench	33
4.5.2	Alignment in-situ	34
4.5.3	Automation of the alignment procedure	35
4.6	Calibration of compensated optical lattice	35
4.6.1	Lattice depth calibration	35
4.6.2	Lattice radial frequency calibration	36
4.6.3	Dimple trap radial frequency calibration	37
4.6.4	Green compensation calibration	38
4.6.5	Summary of lattice calibration	38
4.7	Correction to the peak density measurement	40
4.8	Summary	43
5	Future improvements of the system	45
5.1	Cooling in the compensated lattice	45
5.2	New design of the lattice assembly	47
5.2.1	New lattice assembly	47
5.2.2	Modification to the intensity control system	50
5.3	Summary	51

Bibliography

Illustrations

1.1	Zeeman shift of ${}^6\text{Li}$	3
2.1	Apparatus schematic	5
2.2	Atom sample in a dimple trap	7
3.1	Dual photodiode intensity stabilization scheme	9
3.2	Circuit diagram of high dynamic range intensity servo.	10
3.3	Circuit diagram of photodiode transimpedance amplifier.	12
3.4	Calibration of ODT servo and evaporation trajectory	14
3.5	Noise of ODT intensity feedback loop.	17
3.6	Column density of degenerate Fermi gas after evaporation	19
4.1	Example of compensated potential	24
4.2	Schematic of IR lattice laser setup	26
4.3	Schematic of the green laser system	27
4.4	Schematic lattice assembly design	31
4.5	The overlap of the IR and green beam waists on the test bench	33
4.6	Picomotor movement VS atom cloud size and position offset	34
4.7	Calibration of lattice frequency	36
4.8	Calibration of radial trap frequency of lattice	37
4.9	Calibration of dimple trap frequency	37
4.10	Calibration of green compensation frequency	38

4.11	The 3D density distribution of a Mott and Gaussian distribution . . .	42
4.12	An example for the 2D Mott fit	43
5.1	New Lattice assembly	48
5.2	New servo scheme	50

Tables

4.1	Summary of lattice intensity servo calibration	29
4.2	Summary of lattice calibration (1)	39
4.3	Summary of lattice calibration (2)	39

Chapter 1

Introduction

Optical lattice experiments have proved to be a versatile tool for studying strongly correlated quantum systems. [1,2]. The motivation behind these experiments is that we would like to use cold atom system to emulate an actual solid state system of which the Hamiltonian is analytically or numerically non-solvable [3]. In the experiments for fermions, two hyperfine levels of the ground state of fermionic alkali metal (e.g. ^6Li or ^{40}K [2, 4, 5]) are chosen to represent spin up and down electrons in the real solid state system. The lattice potential is provided by the dipole force potential created by retro reflected laser beams. Along with the tunable interaction between two species of the atom via a Feshbach resonance [6], the optical lattice system gives us full control of the Hamiltonian of interest.

In our experiment, we would like to construct a 3D simple cubic lattice system which would realize the Fermi-Hubbard model and provide us the possibility of studying the antiferromagnetic (AFM) phase. However, to access such phase, the temperature requirement of the system is quite strict [7]. In order to establish evaporative cooling in the optical lattice and to enlarge the size of the AFM phase within the potential, we implement a compensated potential in addition to the standard lattice beam as proposed in [8]. This compensated 3D lattice would not only provide the

possibility of cooling but could also enlarge the AFM phase in the lattice potential.

In this thesis, I will present detailed steps to construct and calibrate the compensated optical lattice system. A brief introduction of important concepts of this experiment will be provided in the following sections.

1.1 Properties of ${}^6\text{Li}$

The ground state and first excited state of ${}^6\text{Li}$ atoms are $1s^22s^1$ and $1s^22p^1$, respectively. The transitions between these two states are called D lines. The fine structure splitting has the form: $E_{so} = \frac{1}{2} \frac{e^2}{4\pi\epsilon_0} \frac{g_s}{2m^2c^2} \langle \frac{1}{r^3} \rangle \vec{S} \cdot \vec{L}$. For ${}^6\text{Li}$, we have two possible excited states which are $J = 1/2$ and $J = 3/2$. And since $l = 0$ for the ground state, there is no fine structure splitting. The transitions $2^2S_{\frac{1}{2}} \rightarrow 2^2P_{\frac{1}{2}}$ and $2^2S_{\frac{1}{2}} \rightarrow 2^2P_{\frac{3}{2}}$ are the D1 and D2 lines. Within each fine structure state, further splitting due to interaction energy of the electron and the nuclear angular momentum is the hyperfine splitting. The hyperfine splitting has the following form: $E_{hs} = A \vec{I} \cdot \vec{J}$. In our experiment, we use the D2 line since it has cycling transitions which are essential for laser cooling. And besides the D2 transition, we also implement a narrow line cooling stage with the transition $2^2S_{\frac{1}{2}} \rightarrow 3^2P_{\frac{3}{2}}$. In the presence of magnetic field, the energy levels shift, as shown in the following diagram.

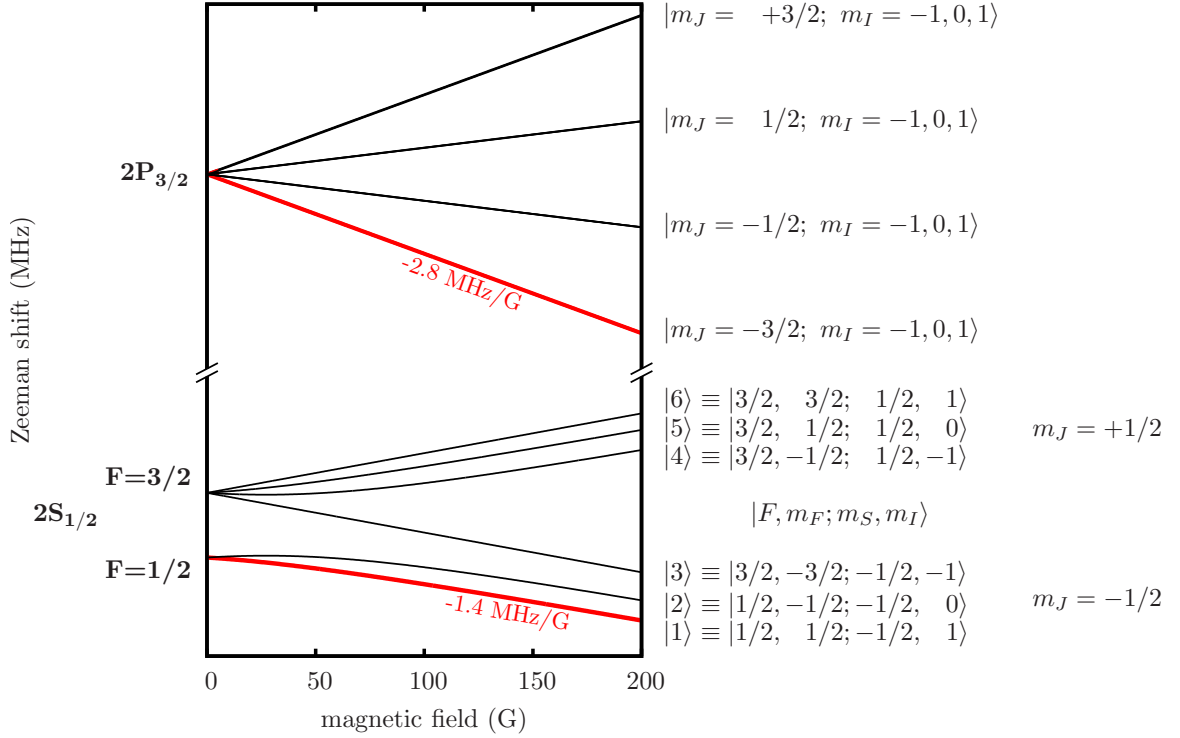


Figure 1.1 : Zeeman shift of ${}^6\text{Li}$. [9]

1.2 Dipole force

The dipole force plays an important role in this experiment. We realize a crossed beam dipole trap and a compensated optical lattice potential via the dipole force. The principle of the dipole force is based on AC Stark shift - the energy level of the atom shifts due to the presence of light intensity. The magnitude and sign of the shift depends on the intensity and detuning of the light. Since we would like to create a conservative potential to trap atoms, far detuned light is chosen to prevent heating

from light scattering. The dipole force can be expressed in the following equation:

$$U_{\text{dip}}(\mathbf{r}) = -\frac{\hbar\Gamma^2}{4} \left(\frac{1}{\omega_0 + \omega} + \frac{1}{\omega_0 - \omega} \right) \frac{I(\mathbf{r})}{I_{\text{sat}}} \quad (1.1)$$

In the case of ${}^6\text{Li}$ with D lines, the saturation intensity $I_{\text{sat}}^{2P} = 5.1 \text{ mW/cm}^2$ and

$\Gamma = 2\pi \times 5.8724 \text{ MHz}$. We can simplify the equation to

$$U_{\text{dip}}(\mathbf{r}) = \alpha_\lambda I(\mathbf{r}) \quad (1.2)$$

In our experiment, we use lasers with, 1064 nm and 532 nm wavelengths. The corresponding α_λ are $\alpha_{1064\text{nm}} = -8.31 \times 10^{-37} (\frac{J}{W/m^2})$ and $\alpha_{532\text{nm}} = 8.48 \times 10^{-37} (\frac{J}{W/m^2})$

1.3 Outline of the thesis

In this thesis, I start by giving a brief review of the experimental sequence in chapter 2. In chapter 3, a detailed description of the high dynamic range intensity stabilization system will be provided. Chapter 4 details the calibration and construction of the compensated optical lattice system. Finally, in chapter 5, the design and considerations for a future improvement of the system will be provided.

Chapter 2

Experimental Sequence

In this chapter, I will present a brief overview of the experiment sequence. For reference, a simplified view of the apparatus can be found in figure 2.1.

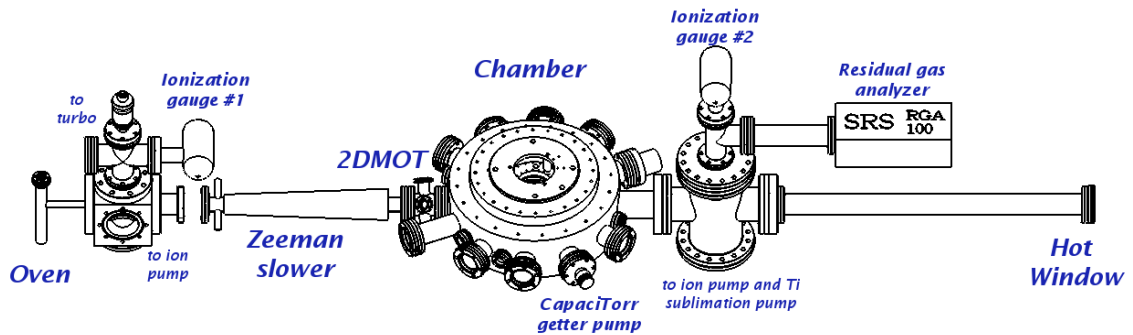


Figure 2.1 : A simplified apparatus schematic. [9]

2.1 Zeeman slower, red MOT, UV MOT

In our experiment, the first cooling stage is the Zeeman slower [10]. The Zeeman slower is a laser beam, red detuned from the $2S_{1/2}, m_J = -1/2$ to $2P_{3/2}, m_J = -3/2$ transition, which propagates in the opposite direction of the hot ${}^6\text{Li}$ atom beam coming out of the oven, see Figure 2.1. A 671 nm MOT is then loaded from the slowed atom beam for around 5 seconds. After cooling and compressing, we have a

cold atom sample with 10^9 atoms at around $350 \mu K$. We then lower the magnetic field gradient to establish narrow line cooling [11,12] with a 323 nm UV MOT, the final temperature of the atom cloud is around $60 \mu K$ and the atom number is around 5×10^8 . At the end of the UV MOT, the magnetic field is switch from gradient to bias field, and the repump laser was turn off early to pump the atoms to the lower hyperfine state.

2.2 Cross-beam dipole trap

The cross-beam dipole trap (ODT) consists of a pair of high intensity 1070 nm laser beams. The two beams cross at 15° with orthogonal polarization. The power of the beams are 39 W for the first path and 35 W for the second path, and the waist of each beam is $73 \mu m$. The ODT is loaded from the UV MOT, and evaporative cooling in the ODT achieves degeneracy of the sample. The typical evaporation time is 6.5 seconds and we can have a degenerate sample with 5.4×10^5 atoms and T/T_{Fermi} equals to 0.18 from an azimuth averaged fit and 0.24 from a 2D Fermi fit. A detailed description of the intensity control of ODT will be provided in chapter 3

2.3 Compensated optical lattice

The dimple trap is formed by three retro reflected 1064 nm lattice beams, but with the input and retro polarization being orthogonal. The polarization of the lattice beams is controlled by a liquid crystal retarder (LCR) before the retro mirror. The

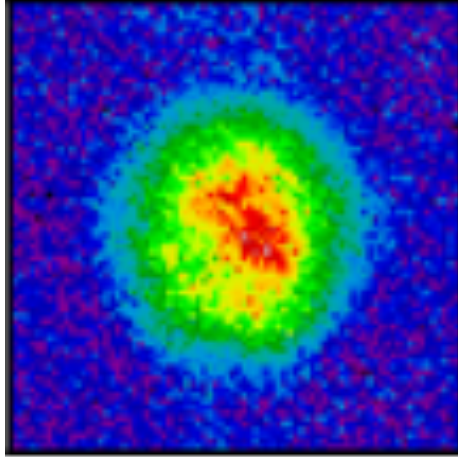


Figure 2.2 : Atom cloud column density in the dimple trap after 0.5 ms time of flight. The atom number is 3.3×10^5 with T/T_F equal to 0.05.

dimple trap is on in the beginning of the ODT evaporation, and at the end of the evaporation we ramp the ODT off in 200 ms and keep evaporating in the dimple trap for an extra 500 ms while holding the dimple trap depth constant. After evaporation in this 1 Er dimple trap, we acquire a degenerate Fermi gas with 3.3×10^5 atoms with T/T_F equal to 0.05. An example can be seen in figure 2.3. We then start to rotate the polarization of the 1064 nm retro laser beams to transform the dimple trap to an optical lattice. At the same time, we ramp up the green and IR laser intensity to the desired compensation and lattice depth and also the field the to desired interaction strength. Once the ramps are finished, we can perform different measurements like measuring the density distribution or measuring Bragg scattering from the sample. More detail about the compensated lattice can be found in chapter 4.

Chapter 3

High dynamic range intensity stabilized dipole trap

The optical dipole trap (ODT) in our experiment is the second cooling stage after the MOT and UVMOT. The ODT is loaded from the UVMOT and evaporation is performed by lowering the intensity of the laser. During the process of evaporation, the laser intensity is slowly ramped down. Since the laser power at the end of evaporation is about 1.5 percent of the power at beginning, using a single photodiode to stabilize intensity will result in a much lower signal to noise ratio at the end of the evaporation trajectory. In order to have efficient noise reduction of the trap depth at both ends of the trajectory, we need a high dynamic range servo system.

3.1 Design and Setup

We implement a dual photodiode scheme to establish a high dynamic range intensity stabilization [13]. The schematic of the setup can be seen in fig 3.1.

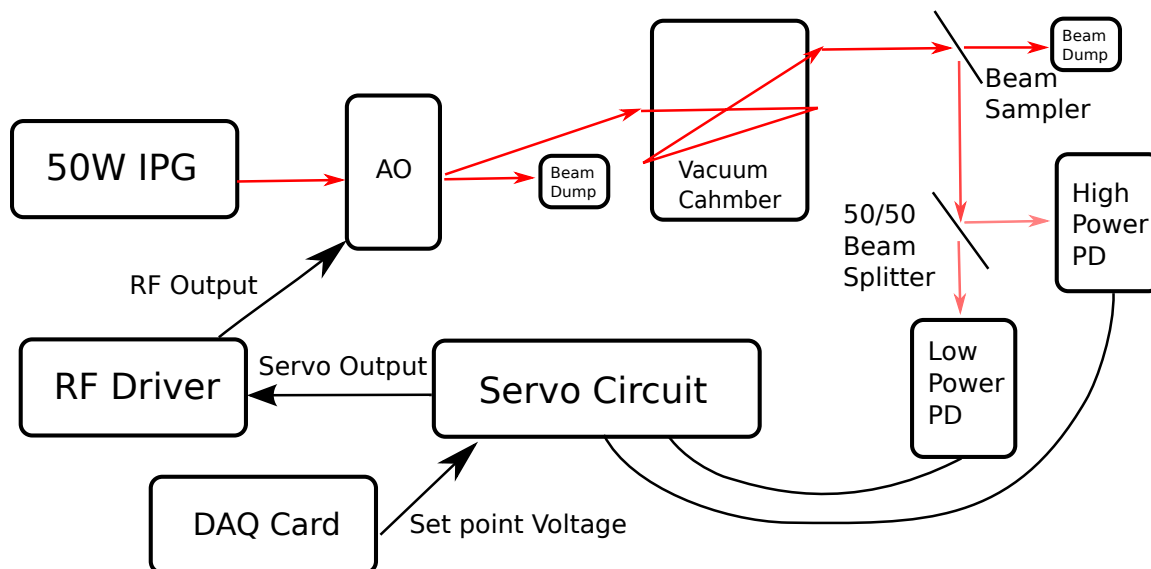


Figure 3.1 : Dual photodiode intensity stabilization scheme.

The basic idea of this dual photodiode scheme is that we feedback control the dipole trap laser intensity on the summed signal of two photodiodes. The intensity of the laser is controlled by the RF power on the acoustic optical modulator (AOM), and the RF power is controlled by a voltage controlled attenuator (VCA). We use one of the photodiodes with low power to voltage gain and one with high power to voltage gain. The photodiode with low gain will not saturate at any level of the laser power during the evaporation and the photodiode with high gain will saturate at certain point. We name these two high power photodiode and low power photodiode, respectively. The summed voltage of these two photodiodes has the feature shown in 3.4(a). If we feedback servo on this signal, we would then have good signal to noise ratio at both low power region and high power region. At the high power region,

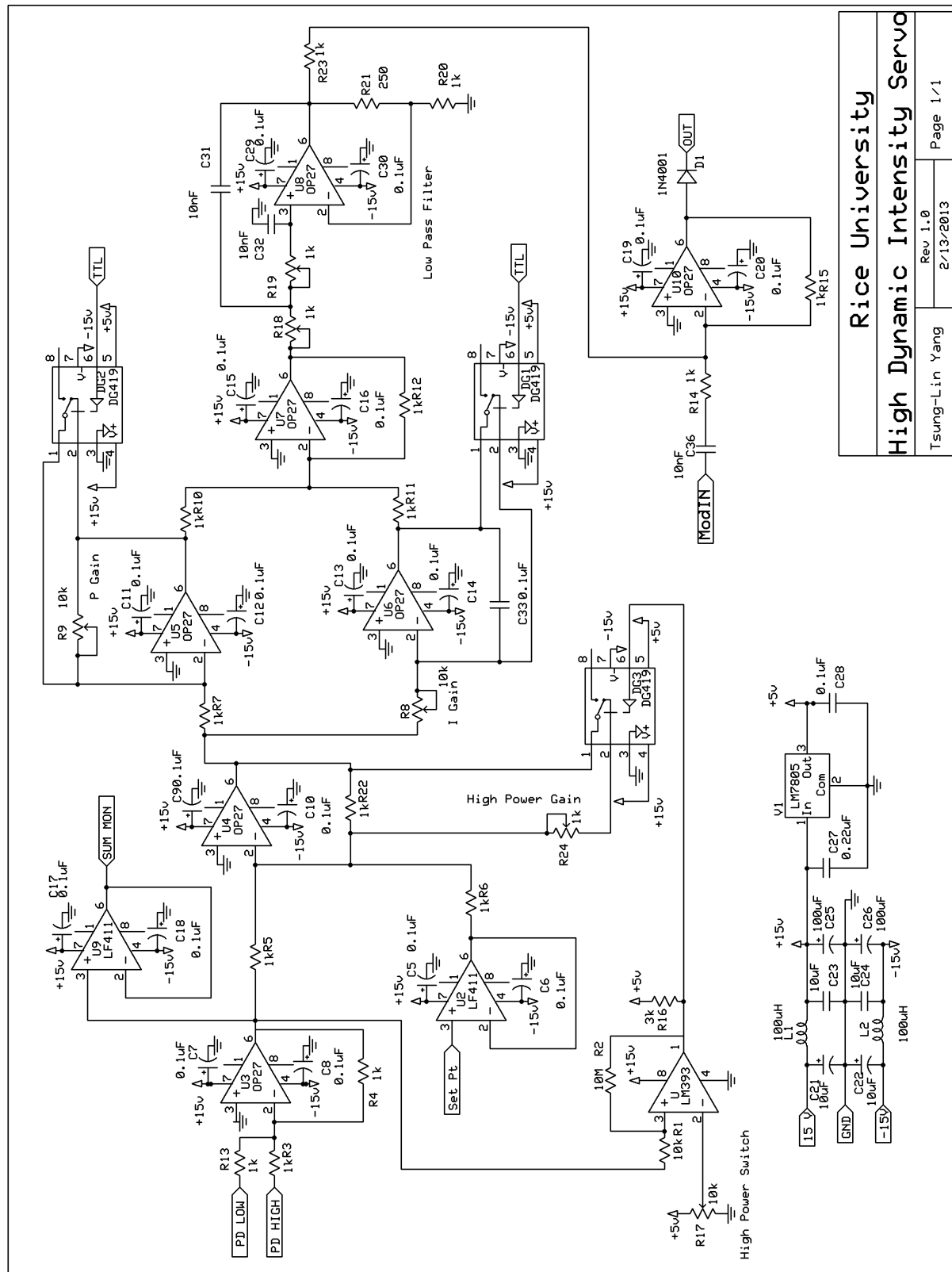


Figure 3.2 : Circuit diagram of high dynamic range insensitivity servo.

the low power photodiode is saturated and we are mainly feeding back with the high power photodiode. At the low power region, where the high power photodiode has really little gain compare to the low power photodiode, the feedback effectively uses only the low power photodiode as the signal.

3.1.1 Gain for the photodiodes

To achieve the best signal to noise ratio on the photodiodes, we would like to put as much light on the photodiodes as possible. The maximum power on each photodiode is chosen as follows: 1. As much power as possible (but lower than damage threshold) at the low power photodiode. 2. Make the power at high power diode just below saturation power. For example, the damage threshold for the the GAP1000 is 100mW and the saturation power for GAP1000 is about 10mW. These two numbers correspond to the ideal setup at the low and high power PD when the trap laser is fully on.

In our setup, the maximum power is ≈ 6 mW on the high power photodiode and is ≈ 80 mW on the low power photodiode. The maximum powers are adjust by neutral density filters in front of the photodiodes. The transimpedance amplifier for both photodiodes was built with 1:3000 current to voltage gain and 2 MHz bandwidth. The circuit digram of the transimpedance amplifier is shown in fig 3.3.

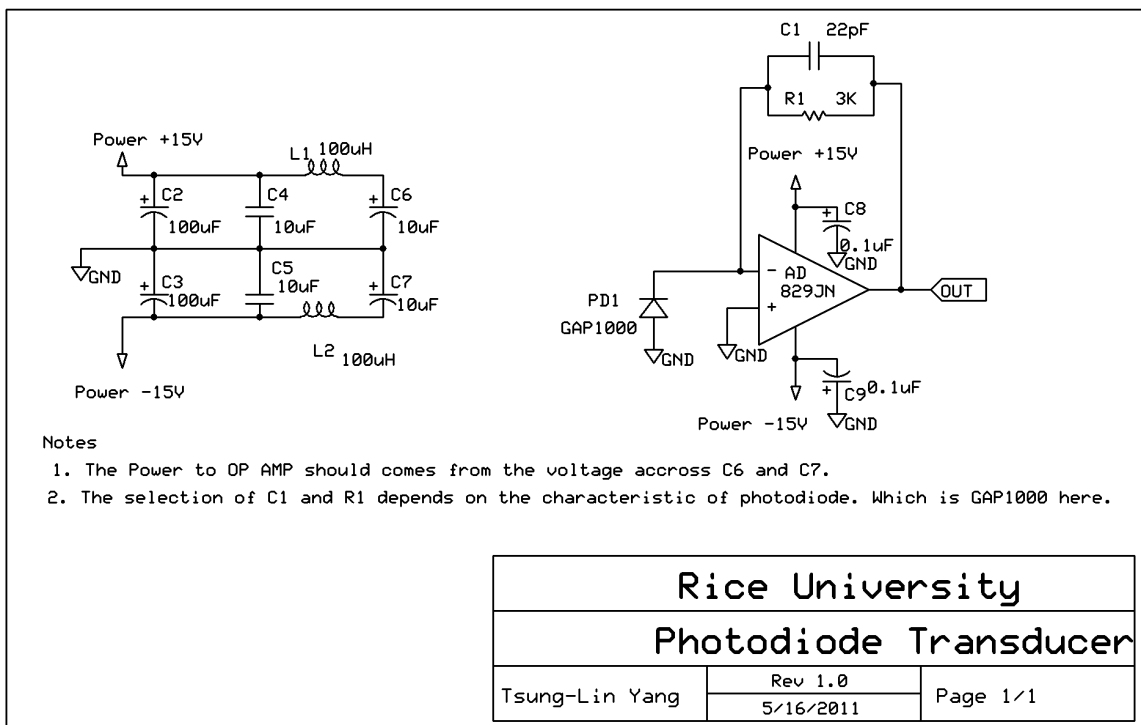


Figure 3.3 : Circuit diagram of photodiode transimpedance amplifier. The bandwidth of the transimpedance amlifier is determined give by $\frac{1}{2 \times \pi R_1 C_1}$ [14]

3.1.2 Calibration of the intensity servo

To calibrate the dual linear curve, we measure both high power photodiode voltage and summed voltage signal when the servo is engaged. Since we know that the voltage from the high power photodiode is linearly proportional to the total power, it serves as a power measurement. We set the set point voltage from the data acquisition card (DAQ) and measure both voltages with an oscilloscope. The measured summed signal and the DAQ set point are slightly offset due to the electronic offset in the output buffer and the servo circuit. However, if we choose the DAQ set point voltage set in the computer as the calibration measurement instead of the measured voltage, the offset can be ignored. We then fit the data with a function:

$$\text{DAQ voltage} = \begin{cases} m_2 \times (\text{Power} - \text{kink}) + m_1 \times \text{kink} + b, & \text{when Power} > \text{kink} \\ m_1 \times \text{Power} + b, & \text{otherwise} \end{cases} \quad (3.1)$$

We then use this calibration function in our sequence directly instead of using interpolation of the data. This saves us time when compiling the evaporation sequence.

3.1.3 PI corner gain for feedback

The feedback control circuit uses a simple PI corner which consists of a proportional gain (P gain) and an integral gain (I gain). In order to achieve optimum feedback gain in the working range of both photodiodes, we also use digital controlled switches (DG419) to switch between two different gain settings. These gain switches are con-

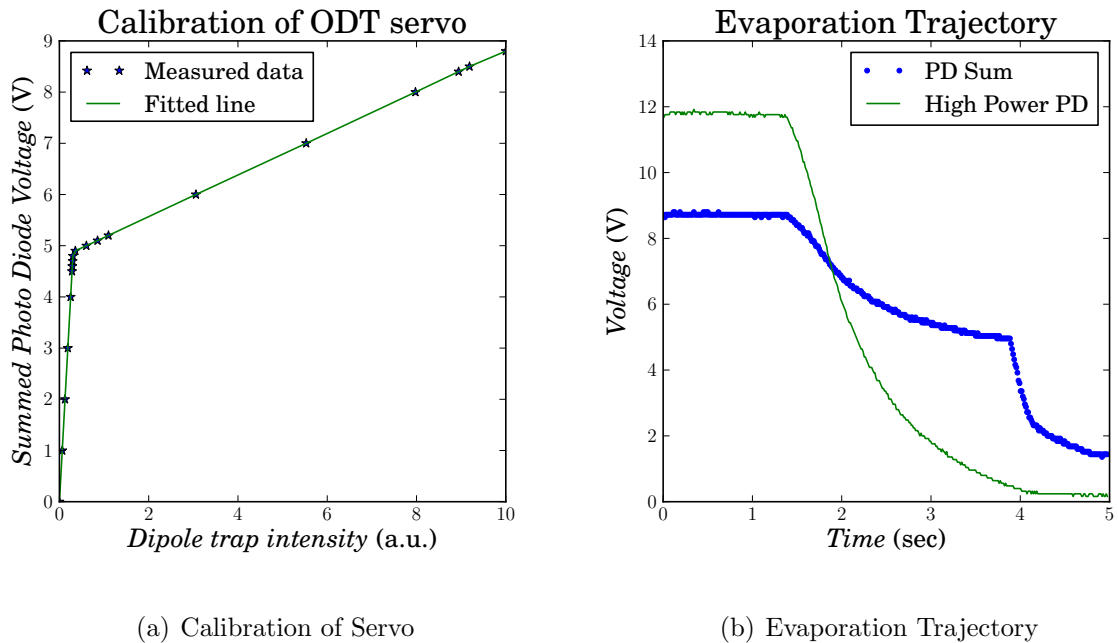


Figure 3.4 : (a): The calibration of the high dynamic servo. (b): The scope trace of the evaporation trajectory. The servo is feedback on the photodiode sum voltage. The high power photodiode voltage is directly proportional to actual power in the dipole trap.

trolled by an output of a comparator, which compares the summed signal and a manual setting voltage value - high gain threshold. When the summed signal goes above the high gain threshold, the DG419 makes one of the the gain resistors be in parallel with an extra potentiometer - this makes the effective gain higher at the high power region.

To set the P and I gains, we first determine the value of P and I gains in the low power region, and then use the extra gain knob described above to set the feedback gain at high power region. During this process, we sweep the set point voltage with a sawtooth wave and with the gains set to minimum and the high gain corner set to maximum - this will make the servo feedback with lower gain throughout the whole

range for now. Then we start increasing the I gain until we see oscillation near the center of the region, where the VAC has highest gain. We then start decrease the I gain until we see no oscillation and keep decreasing the gain to about 50%. We repeat the same procedure with the P gain and decrease to 70% below oscillation. At this point we finished the P and I gain settings for the low power region, and we proceed with the high gain corner. We start by setting the high power gain to maximum and start to decrease the high gain corner and we should see the oscillation start to show up at the top of the curve, we should leave at high gain corner until the oscillation approach the kink of the calibration curve. We then start to decrease the high power gain until we see no oscillation and keep decreasing the gain to about 50% of the value where we stop seeing oscillation.

3.1.4 Bandwidth of the system

The bandwidth of the feedback is limited by the bandwidth of the AOM and the VCA. The AOM we used is 46080-2-1.06 from Neos Technologies. The beam width at the AOM is around $500 \mu\text{m}$. The speed of sound in this AOM is $4.26 \text{ mm}/\mu\text{s}$ and the size of the crystal is 4 mm. With these parameters, we can estimate the rise time and the delay of the modulation. The rise time would be equal to the diameter of the beam divided by speed of the sound in the crystal which is $\frac{500\mu\text{m} \times 2}{4.26\text{mm}/\mu\text{s}} = 0.23 \mu\text{s}$. This gives us the maximum modulation bandwidth $BW = \frac{1}{2 \times \pi \times 0.23\mu\text{s}} = 700 \text{ KHz}$. From the size of the crystal, we can estimate the time delay of the modulation, which is

equal to half the length of the crystal divided by the speed of the sound in the crystal which is $\frac{4mm \times 0.5}{4.26mm/\mu s} = 0.47 \mu s$. Since we can only servo up to the frequency which has less than $\pi/2$ phase delay to the modulation, the maximum bandwidth is $f = \frac{1/4}{0.47\mu s} = 530$ kHz. In this particular case, we can servo up to 530 kHz, and positive feedback would make the servo oscillate beyond this frequency. However, we can still modulate the light up to 700 kHz through the modulation input to the feedback circuit.

The bandwidth of the VCA (Mini-Circuits ZX73-2500+) can be estimated from the rise time (14 μs) and fall time (25 μs). These would give an estimated bandwidth of the VCA of between 6 to 11 KHz. This is the limiting bandwidth of the intensity feedback. Since this is the lowest bandwidth inside the feedback loop, we set the low pass filter in the servo circuit to have a bandwidth 3 kHz. The bandwidth of the entire feedback loop can be seen from the noise measurement fig 3.5.

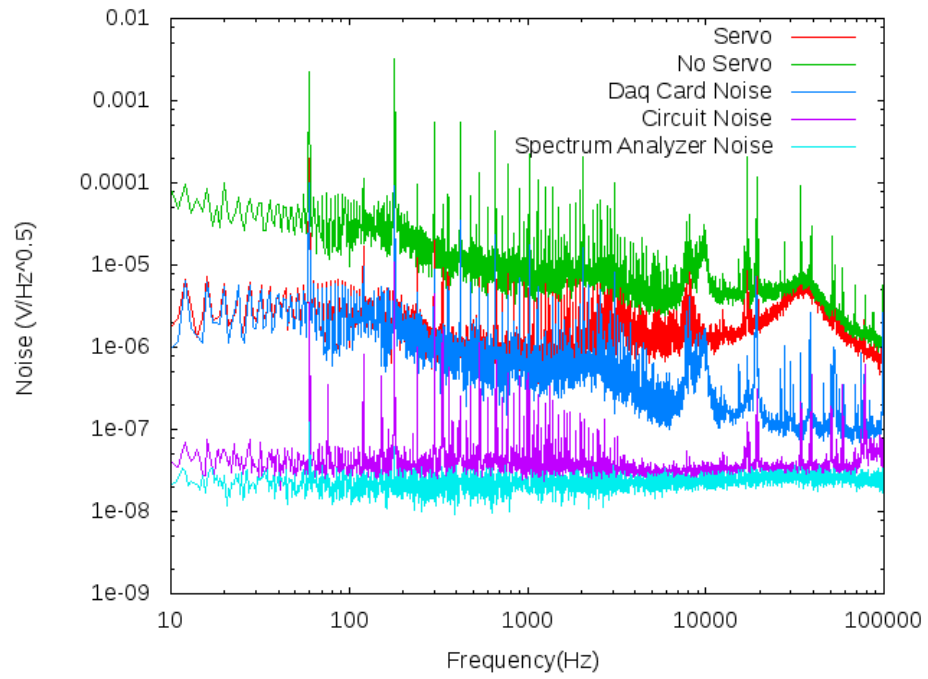


Figure 3.5 : Noise of feedback loop. Noise from the control voltage sets the limit of the servo.

3.1.5 Discussion on noise Source

The circuit noise floor is about $50 \text{ nV}/\sqrt{\text{Hz}}$ (The shot noise of 35 W power is about $100 \text{ nV}/\sqrt{\text{Hz}}$ on the summing output). This is low compared to our laser noise. However, we still can't servo the laser to reach this circuit background noise level. This is because the data acquisition card (DAQ) output noise which we use as the reference voltage of the servo has much higher noise floor than the background of the circuit (see figure 3.5). This noise from the DAQ sets the lowest noise limit to our intensity stabilization. It is possible to filter out the noise by adding a low pass filter to the DAQ card voltage, but it will also decrease the control bandwidth.

3.2 Degenerate Fermi gas

With the high dynamic range control of the dipole trap, we can perform evaporative cooling and reach 5×10^5 atoms at $T/T_f \approx 0.2$ in 6.5 seconds (see fig 3.6). More detailed information can be found in [11] [9].

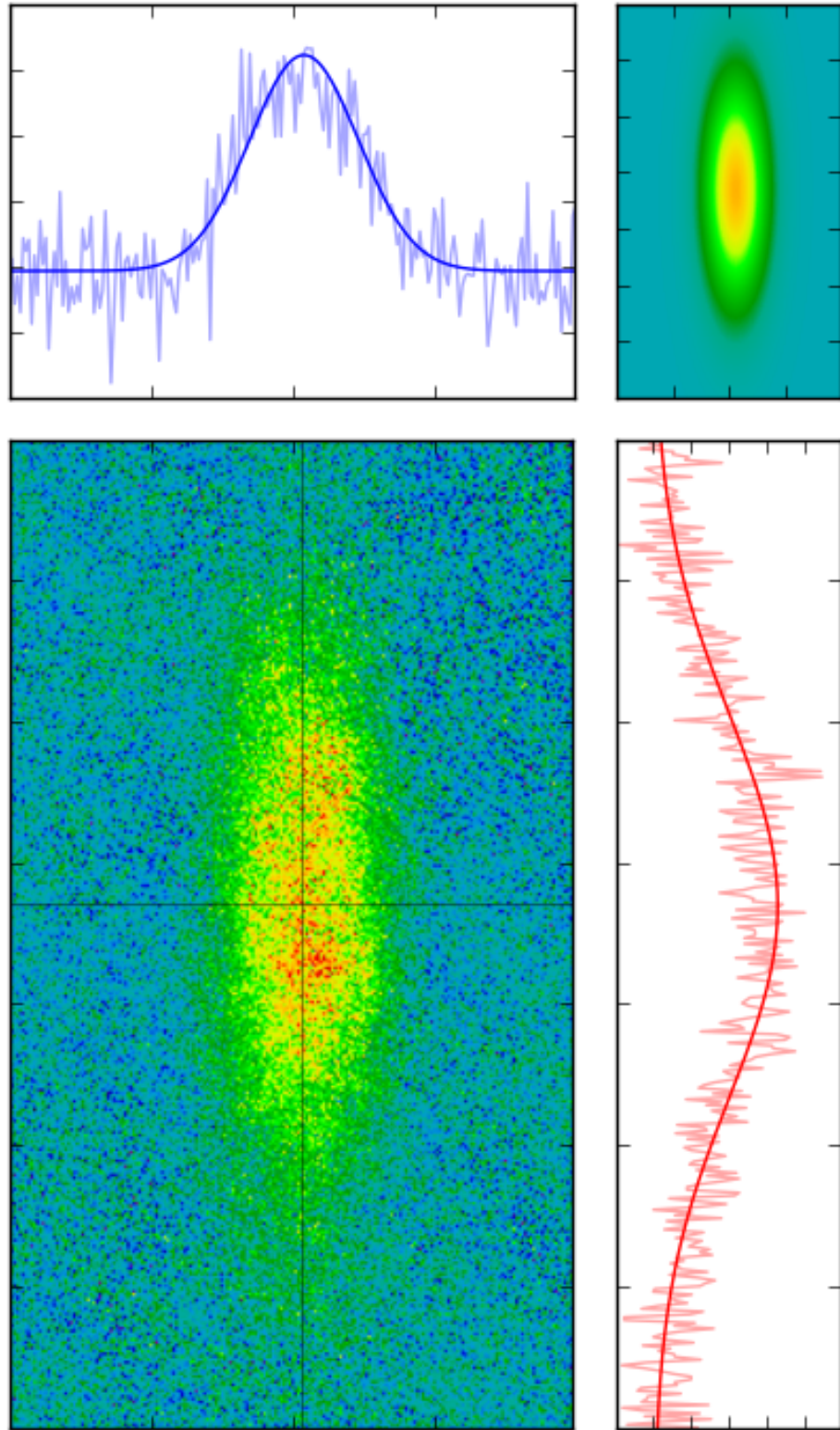


Figure 3.6 : Column density of degenerate Fermi gas after evaporation. The sample after 6.5 second evaporation and with 1.5 ms time of flight. Atom number of the sample is 5.4×10^5 from phase contrast imaging. T/T_F equals to 0.18 from a azimuth averaged fit and 0.24 from a 2D Fermi fit. The azimuth Fermi fit and 2D Fermi fit use an azimuth averaged 1D radial distribution and full 2D distribution, respectively.

Chapter 4

Compensated 3D Lattice

4.1 Introduction to optical lattice

From section 1.2, we know that a red/blue detuned laser beam yields an attractive/repulsive force on an atom that is proportional to the laser intensity. If we retro-reflect the laser beam, the interference of the laser beam would form a periodic intensity pattern with half wavelength spacing. The dipole force of this intensity pattern makes a one dimensional optical lattice and has the following form

$$V(x) = V_x(x) \sin^2\left(\frac{2\pi x}{\lambda}\right) \quad (4.1)$$

With three orthogonal pairs of retro reflected laser beams, we can create a three dimensional optical lattice. The potential would have the following form:

$$V(\vec{r}) = V_x(\vec{r}) \sin^2\left(\frac{2\pi x}{\lambda}\right) + V_y(\vec{r}) \sin^2\left(\frac{2\pi y}{\lambda}\right) + V_z(\vec{r}) \sin^2\left(\frac{2\pi z}{\lambda}\right) \quad (4.2)$$

It should be noticed that the equations above assume that the retro reflected beam has the same intensity and profile as the input beam. If the retro reflected beam has a different intensity profile, we can calculate the total intensity from summing electric fields. For example, we start from a 1D lattice which consists of a retro reflected laser beam with Gaussian beam profile and propagates in the z direction with linear

polarization [15]. We also assume the waist size in x,y directions are the same, then the intensity profile only depends on z and $r \equiv \sqrt{x^2 + y^2}$. We consider only z smaller than the Rayleigh range z_R :

$$I_{\text{inupt}}(z, r) = \frac{\varepsilon_0 c}{2} | E_{\text{inupt}}(z, r) |^2 \quad (4.3)$$

$$E_{\text{inupt}}(z, r) = E_i \frac{w_0}{w(z)} e^{-\frac{r^2}{w(z)^2}} \quad (4.4)$$

$$w(z) = w_0 \sqrt{1 + (z/z_R)^2} \quad (4.5)$$

$$z_R = \frac{\pi w_0^2}{\lambda} \quad (4.6)$$

We now assume the retro reflected beam has the same waist position as the input beams, but with different waist and intensity:

$$E_{\text{total}} = E_{\text{input}} + E_{\text{retro}} \quad (4.7)$$

$$\begin{aligned} V_{\text{IDz}}(z, r) &= \frac{\alpha_\lambda \varepsilon_0 c}{2} (| E_{\text{input}} |^2 + | E_{\text{retro}} |^2 + E_{\text{retro}} E_{\text{input}}^* + E_{\text{retro}}^* E_{\text{input}}) \\ &= \alpha_\lambda (I_{\text{input}} + I_{\text{retro}} + 2\sqrt{I_{\text{input}} \times I_{\text{retro}}} \cos(2kz)) \end{aligned} \quad (4.8)$$

From the equations above we can know that the lattice depth would have the form:

$$V_0 = 4\alpha_\lambda \sqrt{I_{\text{input}} \times I_{\text{retro}}} \quad (4.9)$$

Where α_λ is the dipole force constant, the value of α_λ can be found in section 1.2.

Also, if we expand the intensity near $z = 0$ in the radial direction, we obtain:

$$\begin{aligned}
V_{1Dz}(r, z = 0) \\
= \alpha_\lambda \left[I_{\text{input}} \left(1 - \frac{2r^2}{w_{\text{input}}^2} \right) + I_{\text{retro}} \left(1 - \frac{2r^2}{w_{\text{retro}}^2} \right) + 2\sqrt{I_{\text{input}} \times I_{\text{retro}}} \left(1 - \frac{r^2}{w_{\text{input}}^2} - \frac{r^2}{w_{\text{retro}}^2} \right) \right]
\end{aligned} \tag{4.10}$$

With equation 4.10 and 4.9, we can derive the oscillation radial frequency of the lattice potential and the lattice depth in terms of the power ($P = \frac{\pi w^2}{2} I$) and waists:

$$\nu_{\text{radial}}^2 = \frac{2\alpha_\lambda}{m\pi^3} \left(\frac{P_{\text{input}}}{w_{\text{input}}^4} + \frac{P_{\text{retro}}}{w_{\text{retro}}^4} + \frac{\sqrt{P_{\text{input}} P_{\text{retro}}}}{w_{\text{input}}^3 w_{\text{retro}}} + \frac{\sqrt{P_{\text{input}} P_{\text{retro}}}}{w_{\text{retro}}^3 w_{\text{input}}} \right) \tag{4.11}$$

$$V_0 = \frac{8\alpha_\lambda}{\pi} \frac{\sqrt{P_{\text{input}} \times P_{\text{retro}}}}{w_{\text{retro}} w_{\text{input}}} \tag{4.12}$$

With the 1D potential form equation 4.8, we can now construct a 3D simple cubic lattice by using three orthogonal laser beams:

$$V_{3D}(\vec{r}) = V_{1Dx}(\vec{r}) + V_{1Dy}(\vec{r}) + V_{1Dz}(\vec{r}) \tag{4.13}$$

4.2 Compensated optical lattice

In our experiment, in addition to the retro reflected attractive lattice beams, we also superimpose a non retro-reflected 532 nm laser beam on top of each 1064 nm lattice beam. This co-propagating repulsive laser beam helps cancel the radial harmonic confinement from the lattice beams, eq 4.11, and this enlarges the phase volume in the total potential [7]. The potential created by this repulsive beam propagating in the z direction has the simple Gaussian form:

$$V_{\text{comp}}(\vec{r}) = \alpha_{532nm} \left(\frac{2P}{\pi w(z)^2} \right) e^{-\frac{2r^2}{w(z)^2}} \tag{4.14}$$

The total 1D potential created by a retro reflected lattice beam and a green compensation beam is:

$$V'_{1Dz}(\vec{r}) = V_{1Dz}(\vec{r}) + V_{comp}(\vec{r}) \quad (4.15)$$

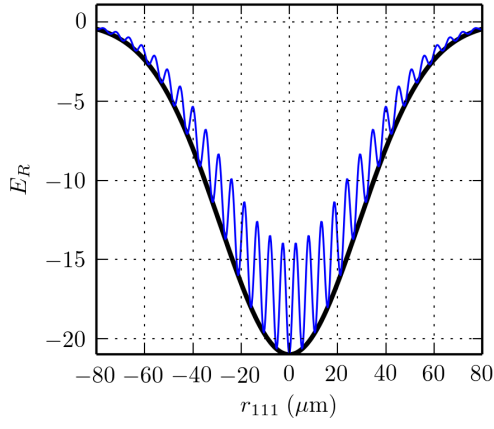
This leads to a reduced radial frequency:

$$\nu_{comp}^2 = \frac{2\alpha_{532nm}}{m\pi^3} \frac{P_{comp}}{w_{comp}^4} \quad (4.16)$$

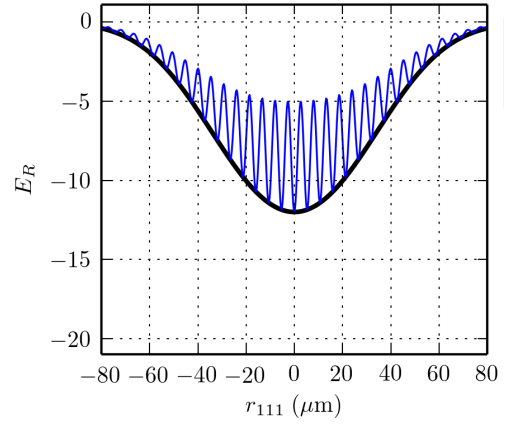
$$\nu_{total}^2 = \nu_{radial}^2 - \nu_{comp}^2 \quad (4.17)$$

And a total 3D potential:

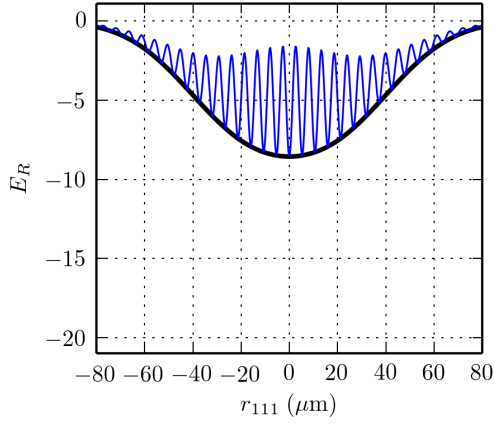
$$V'_{3D}(\vec{r}) = V'_{1Dx}(\vec{r}) + V'_{1Dy}(\vec{r}) + V'_{1Dz}(\vec{r}) \quad (4.18)$$



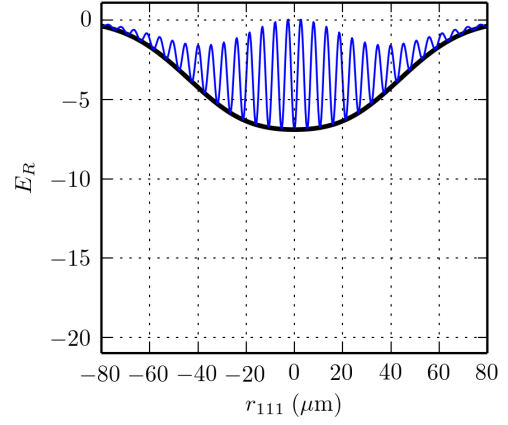
(a) 7 Er lattice, 0 Er green



(b) 7 Er lattice, 3 Er green



(c) 7 Er lattice, 4.15 Er green



(d) 7 Er lattice, 4.7 Er green

Figure 4.1 : These plots show the potential for different amounts of green compensation. The black line is the bottom of the compensated potential and the blue line is the lattice depth. The lattice spacing is scaled up to 10 for these plots. The waist of the lattice beam is $47 \mu\text{m}$ and the waist ratio $\alpha_\omega \equiv \frac{\omega_L}{\omega_C} = 1.17$ as proposed in [8]. Plot (c) shows the compensation when the quadratic part of the band is completely canceled.

4.3 Green and IR laser system

The lasers for the lattice are set on a separate optical table, and the light goes to the apparatus table via fibers. The 1064 nm IR light source is a single mode 35 W IPG fiber laser (YLR-35-1064-LP-SF). The laser is split into three different paths and diffracted by three AOMs. Each AOM controls the intensity sent through each fiber. Similarly, the green compensated light is provided by a 10 W Coherent Verdi laser. And after splitting it in three, the intensity of the beams is controlled by three AOMs. The schematics for the IR and green laser system can be seen in fig 4.2 and 4.3. Each of the three pairs of IR and green beams is combined at the apparatus table by a lattice assembly, which will be described in detail in section 4.4.

4.3.1 Intensity stabilization

The intensity stabilization system of the optical lattice is done by a feedback servo loop which consists of a photodiode and a mixer that controls the RF power to the AOM. It is the same circuit design as for the cross beam dipole trap stabilization described in chapter 3. The only differences in the circuit are that the input comes from a single photodiode, and to control the RF power, we use an RF mixer instead of a VCA, which provides a higher bandwidth of control but requires a rather small control voltage range (0.6 V to 1.2 V). Since we almost always engage the intensity servo of the lattice beams, the small control voltage range is not a problem for us. The position of the photodiodes can be found in section 4.4

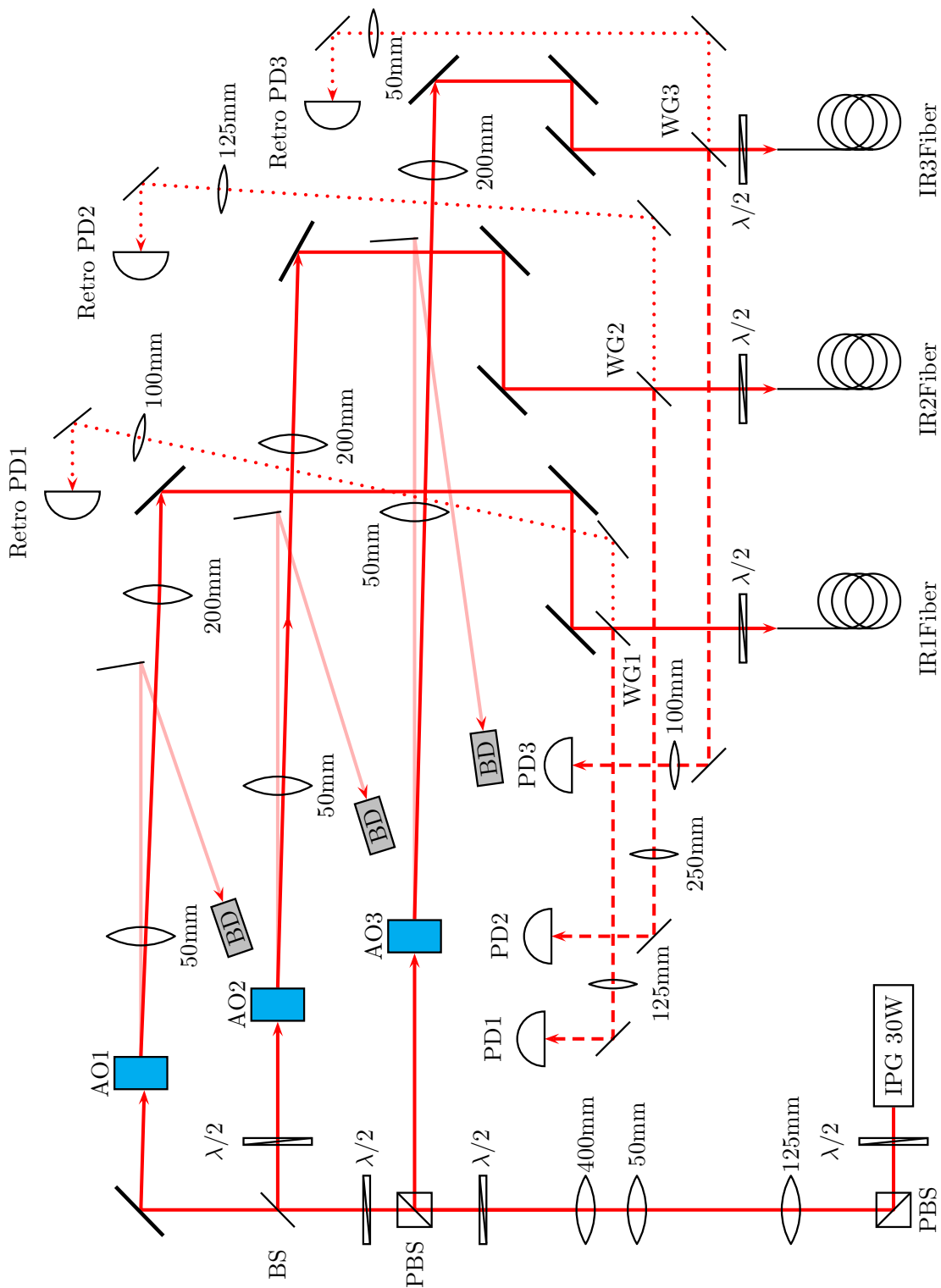


Figure 4.2 : The Schematic of IR lattice laser setup. The IR laser for the optical lattice is a 1064nm 35W single mode fiber laser (YLR-35-1064-LP-SF).

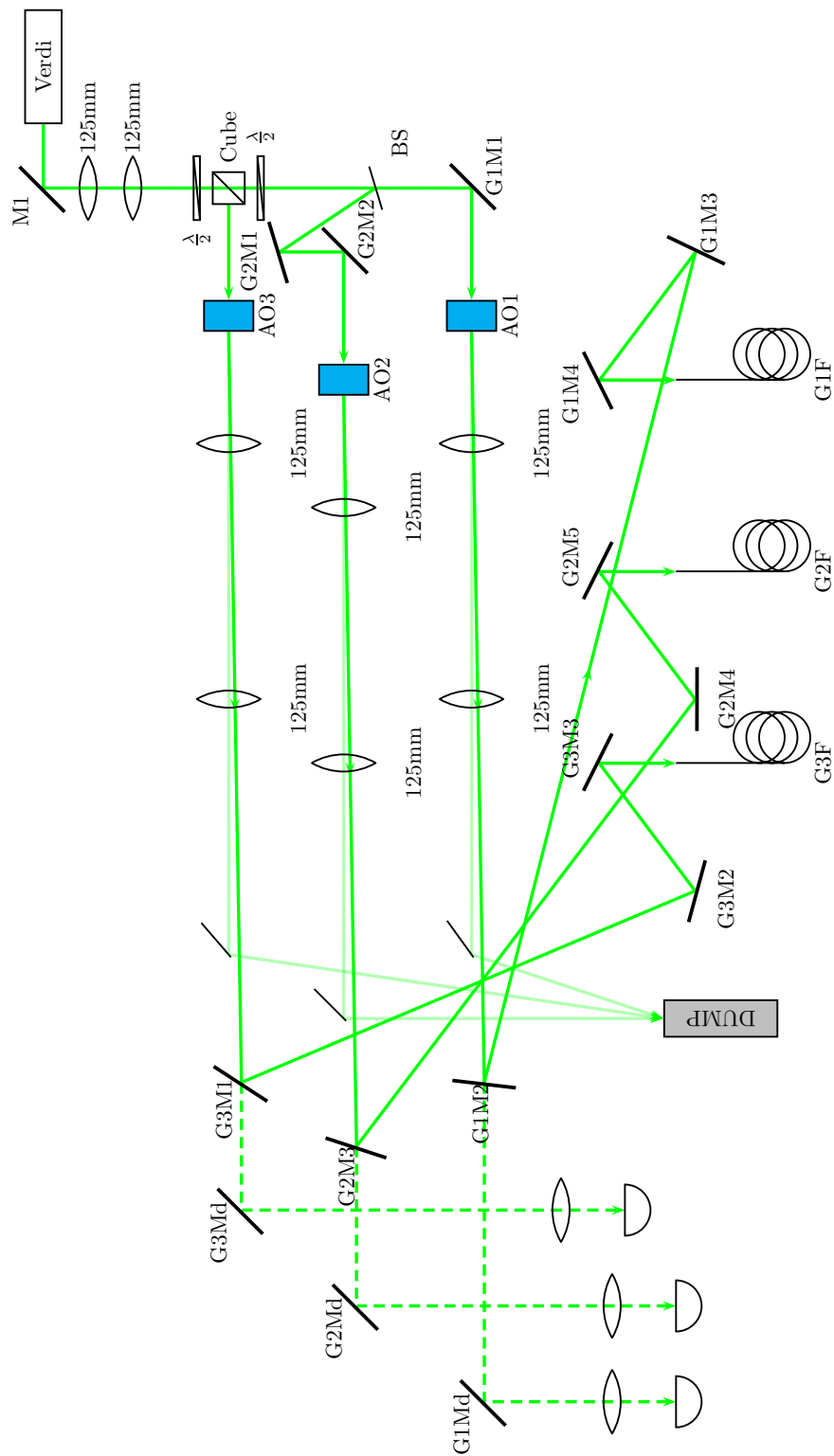


Figure 4.3 : Schematic of the green laser system

4.3.2 Calibration of the intensity servo

The calibration of the intensity servo is done by measuring the photodiode voltage with respect to actual light power. In order to have the best estimate of the light power at the atoms, we measure the power before and after the vacuum chamber and use the average as the power measurement. Since the servo photodiodes are at the end of the light path, we need to disengage the servo circuit when we perform the calibration. With this measurement we can derive the calibration of:

$$V_{\text{photodiode}} = m_1 \times \text{Power} + \text{offset}_1 \quad (4.19)$$

Also, in order to take into account any offset that comes from the measurement device, we perform a calibration of the DAQ set point voltage which is set from the computer with respect to the photodiode voltage when the servo is engaged. Since the servo is engaged, the slope of the measurement is close to 1 and the offset would be on the order of 10 mV.

$$V_{DAQ} = m_2 \times V_{\text{photodiode}} + \text{offset}_2 \quad (4.20)$$

Combining these two equations, we can have the final calibration:

$$\begin{aligned} V_{DAQ} &= m_1 \times m_2 \times \text{Power} + m_2 \times \text{offset}_1 + \text{offset}_2 \\ &= m' \times \text{Power} + \text{offset}' \end{aligned} \quad (4.21)$$

Here is the summary of the calibration of the all the intensity servos:

Table 4.1 : Summary of lattice intensity servo calibration

	IR		Green	
	Slope (V/mW)	Offset(V)	Slope (V/mW)	Offset(V)
Lattice I	4.27e-2	1.35e-2	5.89e-3	3.18e-2
Lattice II	5.07e-3	8.29e-3	4.58e-3	3.19e-2
Lattice III	5.02e-3	-1.70e-3	4.91e-3	1.52e-2

4.3.3 Fiber interlock

In order to prevent the fibers from being damaged by missalignment, we set up an interlock system which monitors the fiber efficiency. For the green laser, since there is no retro reflection back through the fiber, we monitor the power before and after the fiber. And for the IR laser, we monitor the power before the fiber and the power of the retro reflection back through the fiber. If the fiber/retro efficiency drops more than 3%, the interlock turns off the RF driver TTL of the corresponding laser beam and produce a beeping sound for us to know. The lattice fiber interlock circuit uses an arduino micro controller, and a set of AND gates and voltage dividers. The arduino is working as a comparator and a latch for each interlock pair of photodiodes. The output from the Arduino is set to be one of the inputs of an AND gate along with the TTL input from DAQ card to achieve interlock functionality. The reason we use an external AND gate instead of just the arduino is that the arduino has a running cycle of $\approx 2\text{ms}$. If we want to turn on or off the lattice it will have a uncertainty

of 2ms. Using external AND gates avoids this issue. The fiber interlock is really important for our experiment since it not only protects the fibers but also serves as a retro alignment check of the IR lattice beams.

4.4 Lattice Assembly

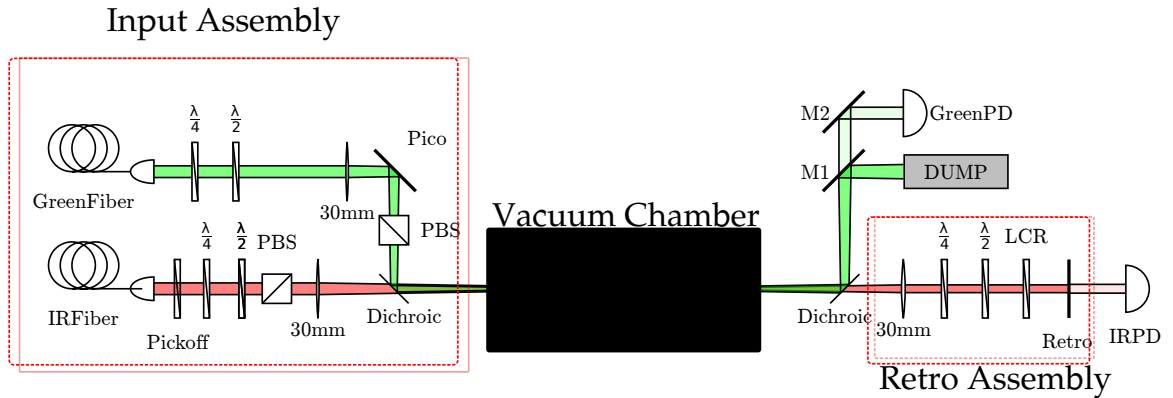
In order to combine each pair of IR and green beams, we designed a lattice assembly to accommodate all the required optics. With this design we can move freely the position of the IR and green pair without affecting the relative position of the two beams. The design of the assembly can be seen in fig 4.4

4.4.1 Picomotor mirror mount

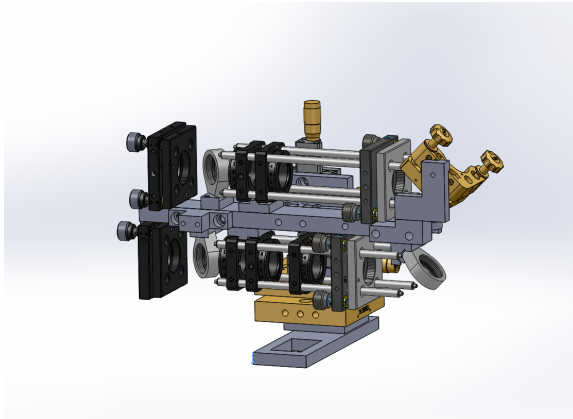
In order to precisely adjust the relative position of the IR and green beam at the atom sample, we implemented a picomotor mirror mount (Model 8807 from Newport) at the mirror which reflects the green beam to the combining dichroic mirror, see fig 4.4(a). This picomotor has $0.7 \mu rad$ step precision. In our system, this gives about $30 \text{ cm} \times 0.7 \mu rad = 0.2 \mu m$ beam movement precision at the atom sample. The waist sizes of the IR and green beams are $45 \mu m$ and $42 \mu m$, respectively.

4.4.2 Liquid crystal retarder

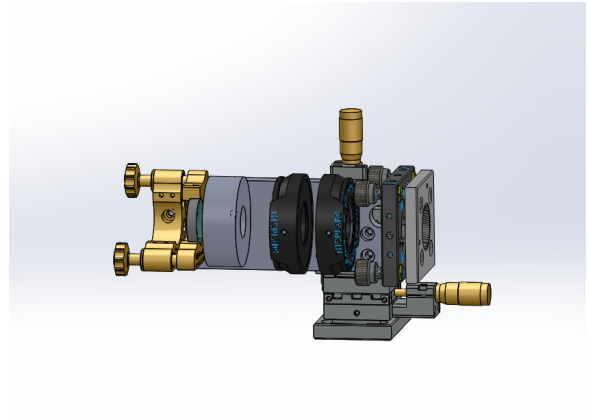
The liquid crystal retarder (LCR) is designed to control the polarization of the retro reflected IR beams [16,17]. With the polarization being parallel to the input beam, we form a optical lattice. With the polarization being orthogonal to the input beam,



(a) Schematic of lattice assembly design



(b) Input Assembly



(c) Retro Assembly

Figure 4.4 : (a): Schematic lattice assembly design: This is the design for our compensated lattice. It should be noted that the beams from lattice assembly for z axis (gravity direction) reflect from a quad-choic mirror before the chamber. The quad-choic mirror reflects 1064 nm IR and 532 nm green light, but passes 671 nm and 323 nm MOT light. And also after the beams pass through the chamber, the beams reflect from another quad-choic mirror before entering the retro assembly. The part number of the quad-choic is BC-WI-5006U-R1064&532/T671&323 from Lambda Research Optics, INC. (b)(c): 3D Solidworks for lattice assembly design

we form a regular dipole trap. It is essential for us to have such control since as we ramp up the lattice potential, we would like to keep the density of the sample constant.

Calibration of LCR

The calibration of the LCR is done by measuring the power at the retro pickoff on the lattice assembly, and since the retro light passes through the polarization cube, the power measurement can be considered as a polarization measurement. We put a 1 Hz voltage ramp to the LCR driver and walk the angle of the half and quarter waveplates on the retro assembly to make the contrast of the pick-off power largest. As we verified on the bench test, where we can pick-off the retro light easily, the polarization extinction ratio at both lattice (same polarization as input) state and dimple (orthogonal polarization with respect to input) state are more than 300:1. And since the response of the LCR is not linear with respect to the control voltage, we use a calibration file and use interpolation to obtain the calibration function.

4.5 Beam Profile and alignment

The alignment of the green and IR beams is sensitive and fragile. Even though we can easily overlap two beams on the test bench, we still need to develop an in-situ alignment procedure after the lattice assemblies are placed in the apparatus.

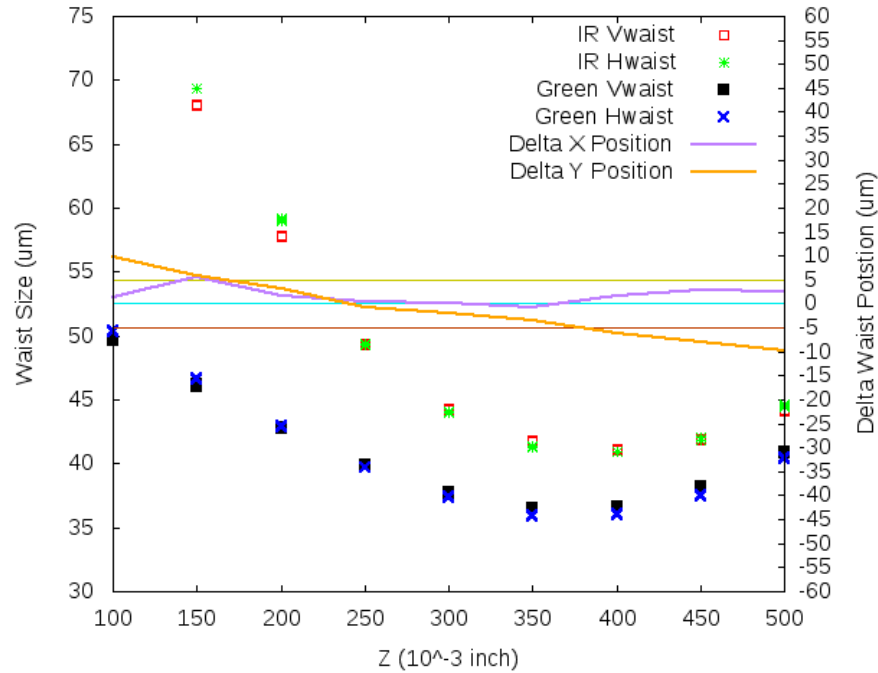


Figure 4.5 : The overlap of the IR and green beam waist on the test bench. The delta X position and delta Y position on the left axis of the plot correspond to the difference of the fitted IR and green beam centers on the CCD camera.

4.5.1 Alignment on the test bench

The alignment on the test bench is done by measuring the two beams directly on a CCD camera. The camera is set on a translational stage which moves the camera along the lattice beam travel direction, i.e. the axial direction. We first align the waist positions along the axial direction of the beams by changing the position of the final lens on the green path. After the waists are at same position in the axial direction, we set the camera at the waist and overlap the beams in the radial direction on the camera. The result is shown in fig 4.5.

4.5.2 Alignment in-situ

After we implemented the assemblies on the apparatus table, the direct measure of the overlap of the beams become impractical. And since the overlap is extremely sensitive to the variation of the environment, we need to check it quite often. To make the process more reliable, we use picomotor mount for the final mirror on each green beam path to achieve fine adjustment of the pointing of the green beams. To align the green beam on top of the IR beam, we use two of the three IR beams to form a lattice sample and use the picomotor to move one of the green beams around to hit the sample. The position of the formed sample will have a dispersive-like curve with respect to the green beam position, and the size of the dimple trap will have a maximum at the same green beam position as the center of the dispersive curve (figure 4.6). We use this information to set the positions of the green beams.

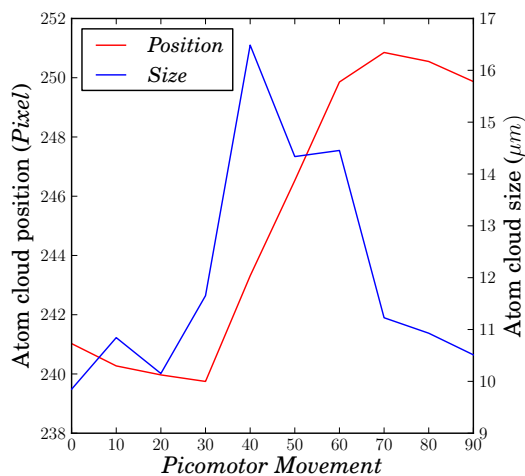


Figure 4.6 : Picomotor movement vs the atom cloud size and position offset

4.5.3 Automation of the alignment procedure

The alignment procedure would usually take about 2 to 3 hours each day, since we need to repeat the same procedure for a total six knobs of the picomotors on the green mirrors. It is quite tedious and time consuming, and sometimes we need to do this more than once a day. In order to reduce the time required, we develop an automatization python script, which will run the required sequences. Based on the results of the analysis, the script overrides the control program through the queue file and the labview control program moves the pico motor accordingly. This automatized system reduces the time required to less than one hour.

4.6 Calibration of compensated optical lattice

From the equations from the previous section we know that to fully calibrate the compensated lattice, we need four different measurements. I will step through the calibration procedures in the following sections. It should be noticed that all the calibration tasks described in this section are done at zero scattering length.

4.6.1 Lattice depth calibration

The lattice depth calibration is achieved by measuring the atom loss in a frequency modulated lattice. The atom loss spectrum reveals a step cut-off frequency which corresponds to the band gap energy difference between 1st and 2nd lattice bands. The energy band gap for a give lattice depth can be calculated numerically. In our

experiment the modulation of the lattice frequency is done by modulating the RF frequency of the acousto-optic modulator for the lattice beams.

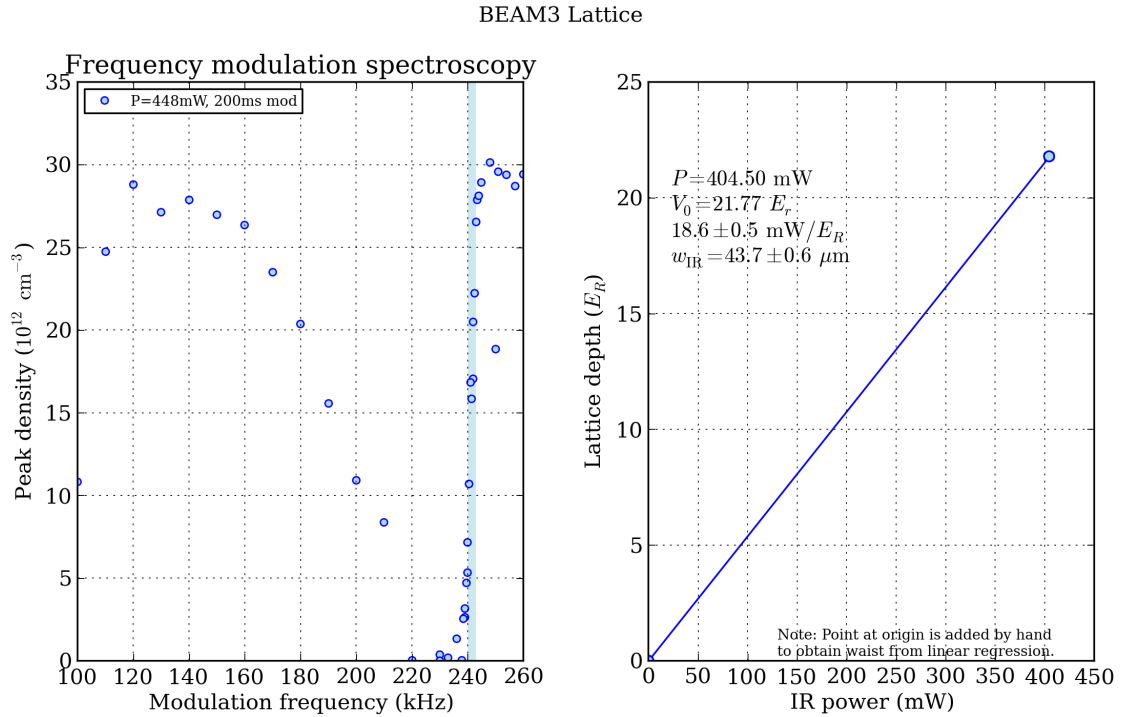


Figure 4.7 : Calibration of lattice frequency.

4.6.2 Lattice radial frequency calibration

Besides the lattice depth, we also measure the radial frequency of the lattice, equation 4.11. The measurement is done by observing the breathing mode oscillation after suddenly turn off the two IR beam pairs other than the beam of interest. With various hold times after the turn off, we can observe the oscillation of the radial size of the atom cloud.

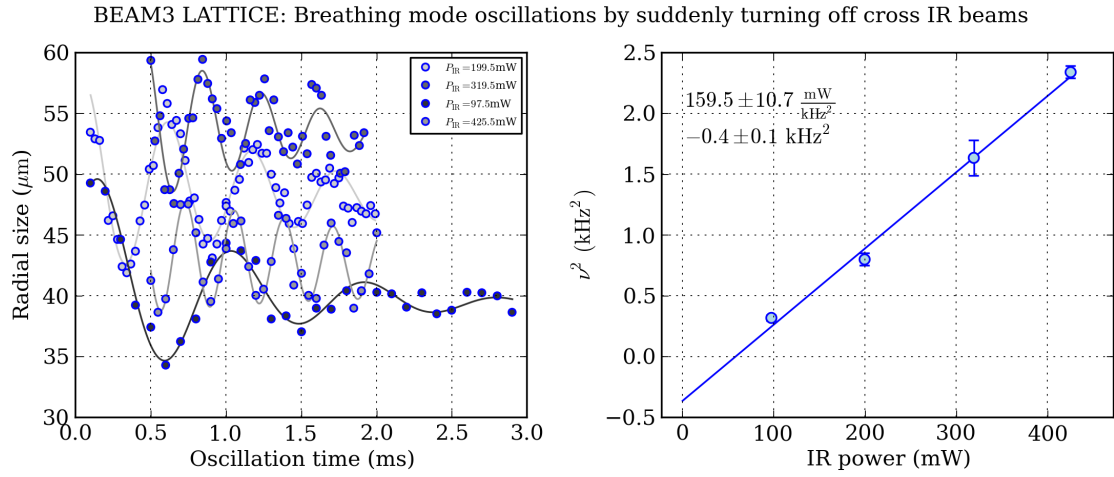


Figure 4.8 : Calibration of radial trap frequency of lattice.

4.6.3 Dimple trap radial frequency calibration

The radial frequency calibration of the dimple trap is done in a similar manner as the lattice radial frequency. And the result can be found in figure 4.9

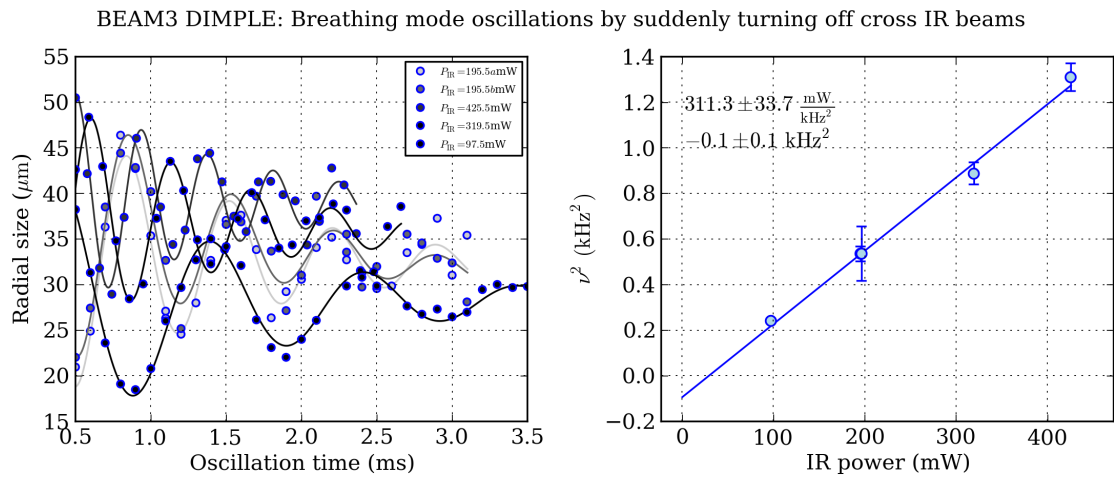


Figure 4.9 : Calibration of dimple trap frequency.

4.6.4 Green compensation calibration

The green compensation is calibrated by measuring the reduction of the radial frequency of the dimple trap with the presence of green light as described by equation 4.17. We first select a certain trap depth of the dimple, and then measure the radial frequency for different amounts of green light power.

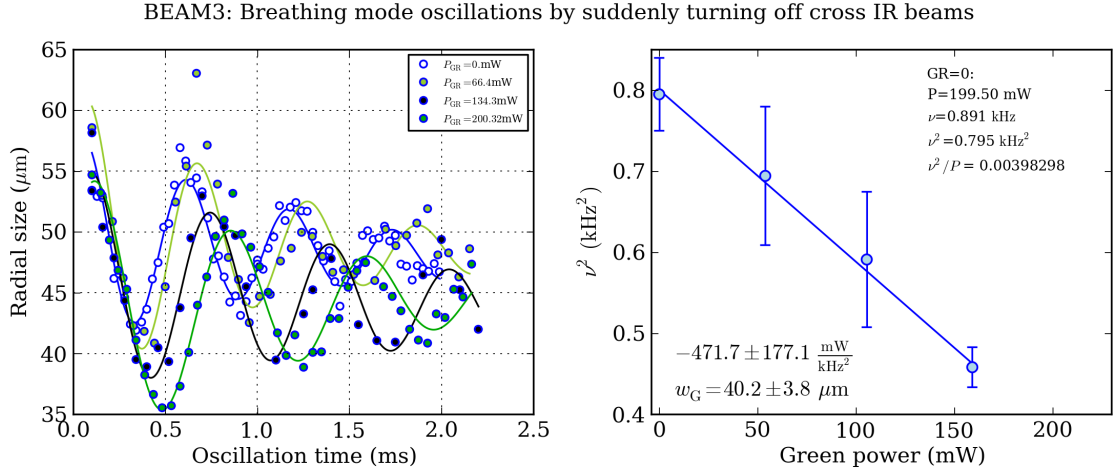


Figure 4.10 : Calibration of green compensation frequency.

4.6.5 Summary of lattice calibration

In the early stage of our experiment, we always tried to set the green compensation power to a fixed depth for all three directions. But the effective potential at the center of the trap not only depends on the trap depth, but also depends on the size of the beam. In our setup, the waist sizes of the green beams have around 10 percent difference. As a consequence, the final compensated sample we had was

always asymmetric. We learned that it not so easy to adjust the ratio of the green power empirically to achieve a symmetrized sample. This prompted us to measure the radial frequencies of the lattice. With this additional measurement, we can assign the combined radial frequency of lattice and green beam to be the same in all three directions. After this adjustment, we can finally achieve a round and symmetric sample. It should be noted that the difference between the waist measured on the bench and derived from calibration comes from that the three lattice beams are not crossed at the focal points.

Table 4.2 : Summary of lattice calibration (1)

	Dimple		Lattice			Green	
	Slope (mw/kHz ²)	Offset (kHz ²)	Slope (mw/kHz ²)	Offset (kHz ²)	Depth (mW/Er)	Slope (mw/kHz ²)	Offset (kHz ²)
I	493.9 ± 27.6	-0.066 ± 0.028	274.6 ± 9.0	-0.13 ± 0.029	21.8 ± 0.3	-607.1 ± 64	0.68 ± 0.023
II	448.7 ± 26.4	-0.083 ± 0.027	239.2 ± 9.9	-0.21 ± 0.041	21.6 ± 0.2	-528.9 ± 42	0.68 ± 0.022
III	315.7 ± 34.6	-0.08 ± 0.12	160.7 ± 11.5	-0.35 ± 0.079	18.6 ± 0.5	-480.3 ± 152.5	0.81 ± 0.086

Table 4.3 : Summary of lattice calibration (2)

	IR		Green	
	Waist from the calibration (μm)	Waist on the bench (μm)	Waist from the calibration (μm)	Waist on the bench (μm)
I	48.3 ± 2.4	39.0 ± 0.27	42.9 ± 1.1	36.5 ± 0.18
II	45.9 ± 2.3	40.5 ± 0.17	41.4 ± 0.8	37.1 ± 0.08
III	41.3 ± 2.1	40.25 ± 0.27	40.4±3.2	34.4 ± 0.03

4.7 Correction to the peak density measurement

We know that at a given chemical potential and large enough interactions, the fermions in a lattice form a Mott insulator. The phase we would like to study, the antiferromagnetic (AFM), is a Mott Insulator [7]. In the Mott insulator phase, the atoms have a density of one particle per site due to the effect of interactions. As a consequence, the density distribution of the atom sample in a lattice potential is different than in a simple harmonic potential. In order to estimate the density distribution better when the atom sample is in the compensated lattice, we developed an empirical column density fit. This empirical model helps us prepare the sample closer to a density one atom per site. An example of this new density fit can be seen in Fig 4.12. We define the density profile of this case as:

$$n(\vec{r}) = \begin{cases} n_0 \cdot e^{-r_d^2} & \text{if } r_d > r_0 \\ n_0 \cdot e^{-r_0^2} & \text{otherwise} \end{cases} \quad (4.22)$$

$$r_d \equiv \left(\frac{x^2}{w_x^2} + \frac{y^2}{w_y^2} + \frac{z^2}{w_z^2} \right)^{\frac{1}{2}} \quad (4.23)$$

Where r_0 is a constant. If $r_0 = 0$, the profile is a regular Gaussian. The column density of it is:

$$n_{col}(x, y) = \int_{-\infty}^{\infty} n(\vec{r}) dz = \begin{cases} w_z \cdot \sqrt{\pi} \cdot n_0 \cdot e^{-r_{xy}^2} & \text{if } r_{xy} > r_0 \\ w_z \cdot \sqrt{\pi} \cdot n_0 \cdot e^{-r_{xy}^2} \cdot [1 - \text{erf}(r_{xy}^*) + \frac{2}{\sqrt{\pi}} \cdot r_{xy}^* \cdot e^{-(r_{xy}^*)^2}] & \text{otherwise} \end{cases} \quad (4.24)$$

$$r_{xy} \equiv \left(\frac{x^2}{w_x^2} + \frac{y^2}{w_y^2} \right)^{\frac{1}{2}} \quad (4.25)$$

$$r_{xy}^* \equiv (r_0^2 - r_{xy}^2)^{\frac{1}{2}} \quad (4.26)$$

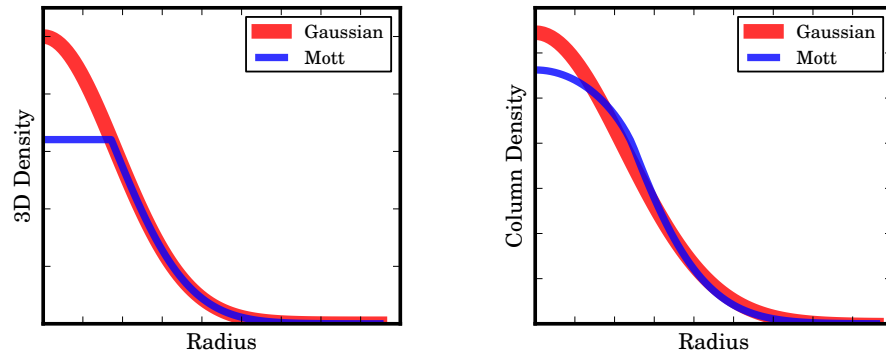
$$\text{erf}(x) = \frac{2}{\sqrt{\pi}} \cdot \int_0^x e^{-t^2} dt \quad (4.27)$$

The peak density and numbers:

$$A \equiv w_z \cdot \sqrt{\pi} \cdot n_0 \quad (4.28)$$

$$n_{peak} = \frac{A \cdot e^{-r_0^2}}{\sqrt{\pi} \times w_z} = \frac{A \cdot e^{-r_0^2}}{\sqrt{\pi} \times \sqrt{w_x w_y}} \quad (4.29)$$

$$N_{tot} = A \cdot \pi \cdot w_x w_y \times \left[1 - \text{erf}(r_0) + \frac{2 \cdot r_0 \cdot e^{-r_0^2}}{\sqrt{\pi}} \left(1 + \frac{2r_0^2}{3} \right) \right] \quad (4.30)$$



(a) 3D Density

(b) Column Density

Figure 4.11 : (a): The 3D density distribution of a Mott (eq 4.22) and Gaussian distribution. (b): The column density of a Mott distributions (eq 4.24) and Gaussian distribution.

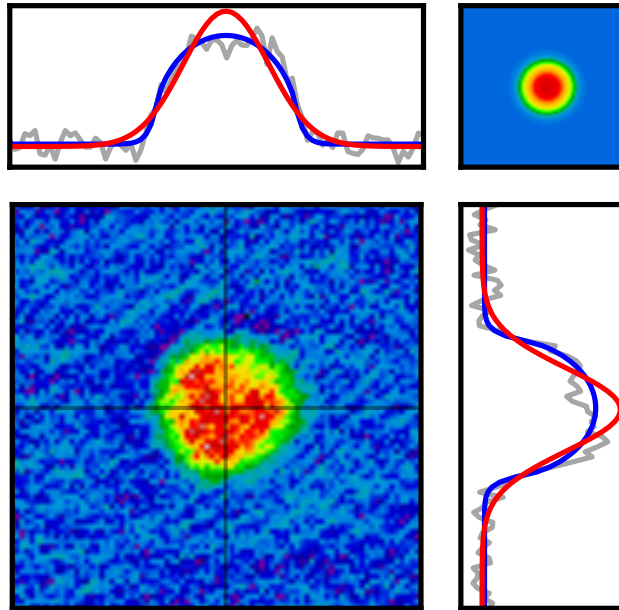


Figure 4.12 : An example for the 2D Mott fit. The plots at bottom left is the column density of the sample in a compensated lattice. The top left and bottom right plots are cuts from the data and the fit. The gray line is the cut form the data; the blue and red line are cuts from a 2D Mott and Gaussain fit. The top right is the column density from a 2D Mott fit. From the plots we can see that the Gaussian fit would over estimate the denstiy at the center of the cloud. The fitted peak density from 2D Gaussian fit is $8.22 \times 10^{12}(cm^{-3})$, but the result from a 2D Mott fit is $4.72 \times 10^{12}(cm^{-3})$

4.8 Summary

With all the calibrations we have presented in this this chapter, and the analysis tools in section 4.7, we have established a 3D compensated simple cubic optical lattice system with all the physical parameters well characterized and controlled. With this system, we can study the many body phase digram of the Fermi-Hubbard model via measuring the Bragg scattering [18]. Also, with the the ability of adjusting the compensation of the potential, evaporative cooling in the lattice could possibly be

achieved. Further study of the Bragg scattering and novel cooling can be found in [19]

Chapter 5

Future improvements of the system

5.1 Cooling in the compensated lattice

In the current setup of the compensated lattice, we chose the beam waist of green and IR to be around $42 \mu m$ and $45 \mu m$, which corresponds to $\alpha_\omega \equiv \frac{\omega_L}{\omega_C} = 1.1$. $\alpha_\omega = 1.1 \sim 1.2$ is proposed in [8] to enlarge the AFM state in the lattice sample. If we consider the lattice potential in 111 lattice direction, the bottom of the lattice potential can be expressed as:

$$V_L(r_{111}) = -3s_0 \exp\left[-\frac{4r_{111}^2}{3\omega_L^2}\right] \quad (5.1)$$

and the compensation potential is:

$$V_C(r_{111}) = 3g_0 \exp\left[-\frac{4r_{111}^2}{3\omega_C^2}\right] \quad (5.2)$$

where s_0 and g_0 is the potential depth create by each lattice and compensation beam.

Also consider the band structure, the bottom of the band will has the form:

$$E_0 = \frac{3}{2}\hbar\omega_0 = 3\sqrt{s} \quad (5.3)$$

where s is the lattice depth in the unit of recoil energy. The lowest band profile expanded for r_{111} near zero:

$$E_0 \approx 3(g_0 + \sqrt{s_0} - s_0) + \left(\frac{4s_0 - 2\sqrt{s_0}}{\omega_L^2} - \frac{4g_0}{\omega_C^2}\right)r_{111}^2 + \left(\frac{-8s_0 + 2\sqrt{s_0}}{3\omega_L^4} + \frac{8g_0}{3\omega_C^4}\right)r_{111}^4 + O(r_{111}^6) \quad (5.4)$$

If we considering cancel the quadratic term for a given α_ω , we would need $g_0 = \frac{s_0}{\alpha_\omega^2}(1 - \frac{1}{2\sqrt{s_0}})$. In the approximation for deep lattice, the remaining potential would be:

$$E_0 \approx 3s_0\left(\frac{1}{\alpha_\omega^2} - 1\right) - \frac{8s_0}{3\omega_L^4}(1 - \alpha_\omega^2)r_{111}^4 + O(r_{111}^6) \quad (5.5)$$

It can be seen from the first term of equation 5.5, the bottom of the band would be higher with a lower α_ω . In the consideration of evaporation at a given chemical potential, we would like a smaller α_ω to have the chemical potential near the top of the trap. For a quick estimate for the required chemical potential for a 1 per site density:

$$\mu \approx E_F = \frac{\hbar^2}{2m}(3\pi^2 n)^{\frac{2}{3}} \quad (5.6)$$

$$\frac{E_F}{E_{recoil}} = \frac{\frac{\hbar^2}{2m}(3\pi^2/d^3)^{\frac{2}{3}}}{\frac{\hbar^2}{2m}\left(\frac{2\pi}{2d}\right)^2} \approx 1 \quad (5.7)$$

where n is the density, d is the lattice spacing and E_F is the Fermi energy. This also sets the limit that the bottom of the band should be smaller than -1 E_r . Also, in order to have a confining quartic potential we would need α_ω to be greater than one. In order to explore these trade-offs, we would like to gain control of the waist ratio between IR and green beams. However, in the current setup, the waist sizes of the

beams are fixed. In order to gain control of the waist ratio, we would like to build up an improved compensated lattice system presented in the following section.

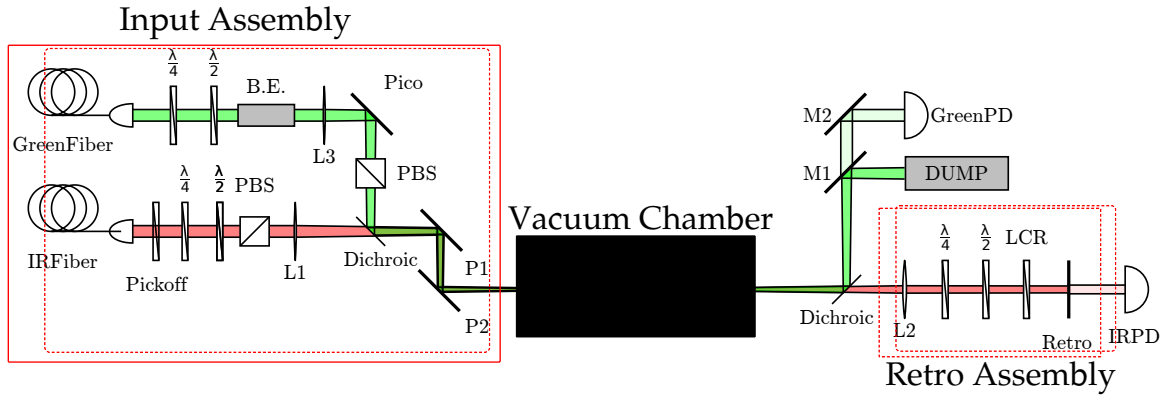
5.2 New design of the lattice assembly

The new design of the lattice setup will consist of two parts: 1, new design of the lattice assembly. 2, new intensity control scheme. The details of these two parts will be provided in the following sections.

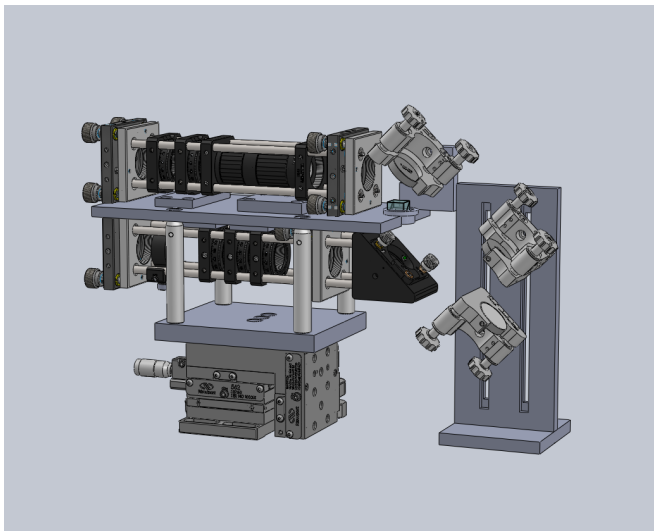
5.2.1 New lattice assembly

Translational stage and tilt stage

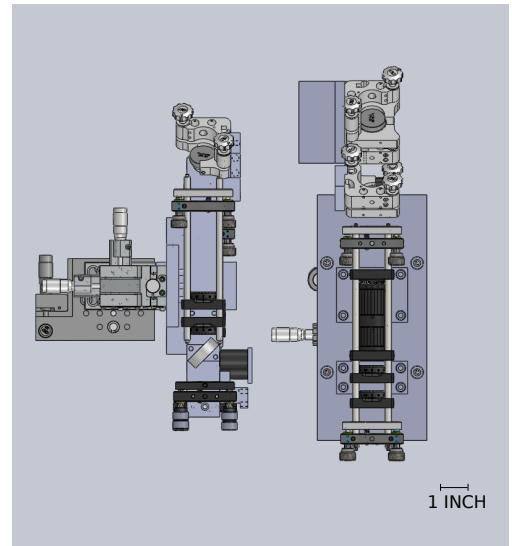
In the current design, the entire assembly hangs off the side of the translational stage. Although the weight of the assembly (around 5 lbs) is less than the maximum load capacity (8 lbs), it is still close to the limit. The tilt stage under the translational stage makes the current assembly bulky and occupies a lot of space on the experiment table. In the new design, we choose a different type of translational stage (Newport 562-XYZ) which has a much higher maximum load (35 lbs). Also since the new stage sits under the optics, the new assembly would be more compact overall (figure 5.1(c)). In the current design, the tilt stage is used to correct the angle of the combined lattice beams. In order to gain more flexible control of the pointing, a periscope is used instead of the tilt stage. The periscope is separate from the main assembly to reduce the load on the translational stage (figure 5.1(b)). Finally, an adjustable mount for



(a) Schematic of new lattice assembly design



(b) Input Assembly



(c) Top view of old and new assembly

Figure 5.1 : (a):The schematic of new lattice assembly design. A beam expander (BE) is implemented to provide the ability to change the waist size ratio. A pair of mirrors (P1 and P2) are used to adjust the pointing of the lattice beams, and an adjustable mount for the dichroic mirror replaces the fixed mount to provide relative angle adjustment between the IR and green beams. (b): 3D drawing of the new lattice assembly. (c) Comparison between old (left) and new (right) assembly. It can be seen that the new assembly is more compact and occupies less space on the experiment table.

the dichroic mirror replaces the fixed mount to provide relative angle adjustment between the IR and green beams.

Beam Expander

From the discussion from previous sections, we know that in order to achieve better evaporation, we need to set the size of the compensating green beam closer to the lattice beam. The current waists of the compensation and lattice beams are $36 \mu m$ and $40 \mu m$ measured by CCD camera directly. In order to investigate the effect of different beam waists, we need to redesign the lattice assembly to enable the possibility of changing the relative waist size of the two beams. Although we could change the waist size by changing the position of the focusing lens, it will also change the axial overlap with the lattice beam. In order to achieve such requirement, we can implement a telescope in the compensation beam path before the beam reaches the focusing lens. The current beam waist before the focusing lens is 1.4 mm . We can estimate the waist size at the focus from the formula:

$$w = \frac{\lambda}{\pi} \times \frac{F}{w_0} \quad (5.8)$$

where F is the focal length, w_0 is the waist at the lens, and w is the waist at the focal point. The current setup and this formula give us a waist at the focal point of about $36 \mu m$. With a 0.5x to 2x beam expander (BE052-A from Thorlab), we could easily adjust the waist at the focal point from 18 to $72 \mu m$. Further bench tests need to be done for the stability of such beam expanding system. If the mechanism of the

expander is not stable enough, we can replace the expander with a pair of lenses.

5.2.2 Modification to the intensity control system

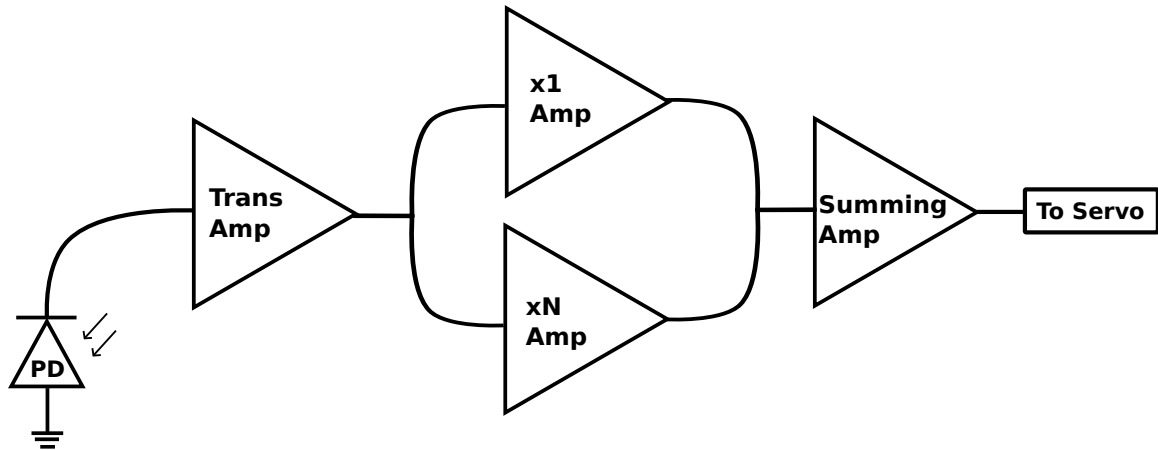


Figure 5.2 : Using a single photodiode to achieve high dynamic range intensity stabilization. By adjusting the gain of the xN amplifier, we can adjust low power gain of the dual linear response (figure 3.4(a)). It should be remembered that the effective noise of the gain signal should be kept below the control voltage noise (figure 3.5)

As we run the Bragg scattering experiment, we need to lock the lattice depth before exposing the Bragg light to achieve the largest possible Debye-Waller factor. Typical locking lattice depth is from 20 to 40 E_r . This high lattice depth requirement makes the initial loading to a 1 E_r dimple trap power to have relatively low control voltage (on the order of 100 mV). Ideally, with the intensity control system we built, we can control the intensity well even in this low voltage range. However, the offset in the experiment could have up to $\sim 10mV$ uncertainty from day to day. This drift will affect the atom number in our final lattice sample. In order to overcome this issue, a similar system as described in chapter 3 needs to be implemented on the

lattice intensity servos. Although we can use the identical dual photodiode scheme, the space on the experiment table is quite tight. However it turns out that if we use the existing photodiode and use a summing amplifier with different gains, we can achieve a non-linear power to voltage response identical to the one shown in 3.4(a). This scheme would have more voltage noise when we are at the low power region, but as we can see from the noise spectrum (see figure 3.5), even if we gained up the photodiode amplifier by 10 times, the noise level would still be below the DAQ card noise level. This will give us a high dynamic range intensity control without modifications to the current setup on the experiment table. A simplified schematic is provided in figure 5.2.

5.3 Summary

With the modification and improvement describe in section 5.2, we can control the relative waist size of our compensated 3D optical lattice system which could lead to better evaporation in the lattice. And with the better intensity stabilization proposed in section 5.2.2, we can have a better day to day stability of the lattice potential control. The next generation system with these improvements could provide us the possibility of cooling the system further toward the Néel temperature.

Bibliography

- [1] M. Greiner, O. Mandel, T. Esslinger, T. W. Hänsch, and I. Bloch, “Quantum phase transition from a superfluid to a Mott insulator in a gas of ultracold atoms,” *Nature*, vol. 415, pp. 39–44, Jan. 2002.
- [2] R. Jördens, N. Strohmaier, K. Günter, H. Moritz, and T. Esslinger, “A Mott insulator of fermionic atoms in an optical lattice,” *Nature*, vol. 455, pp. 204–7, Sept. 2008.
- [3] R. P. Feynman, “Simulating physics with computers,” *International Journal of Theoretical Physics*, vol. 21, pp. 467–488, June 1982.
- [4] U. Schneider, L. Hackermüller, S. Will, and T. Best, “Metallic and insulating phases of repulsively interacting fermions in a 3D optical lattice,” *Science*, vol. 322, no. December, pp. 1520–1525, 2008.
- [5] U. Schneider, *Interacting Fermionic Atoms in Optical Lattices*. PhD thesis, 2010.
- [6] C. Chin, R. Grimm, P. Julienne, and E. Tiesinga, “Feshbach resonances in ultracold gases,” *Reviews of Modern Physics*, vol. 82, pp. 1225–1286, Apr. 2010.
- [7] C. Mathy and D. Huse, “Accessing the Néel phase of ultracold fermionic atoms

- in a simple-cubic optical lattice,” *Physical Review A*, vol. 79, p. 063412, June 2009.
- [8] C. J. M. Mathy, D. a. Huse, and R. G. Hulet, “Enlarging and cooling the Néel state in an optical lattice,” *Physical Review A*, vol. 86, p. 023606, Aug. 2012.
- [9] P. M. Duarte, “Narrow line laser cooling of lithium : A new tool for all-optical production of a degenerate Fermi gas,” Master’s thesis, 2011.
- [10] C. J. Foot, “Laser cooling and trapping of atoms,” *Contemporary Physics*, vol. 32, pp. 369–381, Nov. 1991.
- [11] P. M. Duarte, R. a. Hart, J. M. Hitchcock, T. a. Corcovilos, T.-L. Yang, a. Reed, and R. G. Hulet, “All-optical production of a lithium quantum gas using narrow-line laser cooling,” *Physical Review A*, vol. 84, p. 061406, Dec. 2011.
- [12] D. C. McKay, D. Jervis, D. J. Fine, J. W. Simpson-Porco, G. J. a. Edge, and J. H. Thywissen, “Low-temperature high-density magneto-optical trapping of potassium using the open 4S5P transition at 405 nm,” *Physical Review A*, vol. 84, p. 063420, Dec. 2011.
- [13] J. Fuchs, *Molecular Bose-Einstein Condensates and p-wave Feshbach Molecules of ${}^6\text{Li}_2$* . PhD thesis, 2009.
- [14] J. Graeme, “Photodiode Amplifiers,” 1996.

- [15] B. E. A. Saleh and M. C. Teich, *Fundamentals of Photonics*. Wiley Series in Pure and Applied Optics, New York, USA: John Wiley & Sons, Inc., Aug. 1991.
- [16] T. Paprotta, “A 2D Optical Lattice for Creating a 1-Dimensional Fermi Gas by in Partial Fulfillment of the Requirements for the Degree Master of Science by,” Master’s thesis, 2009.
- [17] Y. Liao, *Strongly Interacting Fermi Gases in 3D and 1D*. PhD thesis, 2011.
- [18] T. a. Corcovilos, S. K. Baur, J. M. Hitchcock, E. J. Mueller, and R. G. Hulet, “Detecting antiferromagnetism of atoms in an optical lattice via optical Bragg scattering,” *Physical Review A*, vol. 81, p. 013415, Jan. 2010.
- [19] P. M. Duarte, *TBD*. PhD thesis, 2014.
- [20] K. OHara, M. Gehm, S. Granade, and J. Thomas, “Scaling laws for evaporative cooling in time-dependent optical traps,” *Physical Review A*, vol. 64, p. 051403, Oct. 2001.